

# Characteristics of Kelvin-Helmholtz Waves as Observed by the MMS from September 2015 to March 2020

Rachel Rice<sup>1</sup>, Katariina Nykyri<sup>1</sup>, Xuanye Ma<sup>1</sup>, Brandon Burkholder<sup>2</sup>

<sup>1</sup>Embry-Riddle Aeronautical University, Department of Physical Sciences, Center for Space and  
Atmospheric Research

<sup>2</sup>University of Maryland Baltimore County, Goddard Planetary Heliophysics Institute

## Key Points:

- A survey of MMS data from September 2015 to March 2020 identified 45 Kelvin-Helmholtz wave events.
- Events are observed for the full range of solar wind conditions. Growth rates are independent of solar wind conditions.
- A new method is developed for the automatic detection of magnetosheath and magnetospheric regions within the KHI.

## 14 **Abstract**

15 The Magnetospheric Multiscale (MMS) mission has presented a new opportunity to study  
 16 the fine scale structures and phenomena of the Earth’s magnetosphere, including cross  
 17 scale processes associated with the Kelvin-Helmholtz Instability (KHI), but such stud-  
 18 ies of the KHI and its secondary processes will require a database of MMS encounters  
 19 with Kelvin-Helmholtz (KH) waves. Here we present an overview of 45 MMS observa-  
 20 tions of the KHI from September 2015 to March 2020. Growth rates and unstable solid  
 21 angles for each of the 45 events were calculated using a new technique to automatically  
 22 detect plasma regions on either side of the magnetopause boundary. There was no ap-  
 23 parent correlation between solar wind conditions during the KHI and its growth rate and  
 24 unstable solid angle, which is not surprising as KH waves were observed downstream of  
 25 their source region. We note all KHI were observed for solar wind flow speeds between  
 26 295 km/s and 610 km/s, likely due to a filtering effect of the instability onset criteria and  
 27 plasma compressibility. Two-dimensional Magnetohydrodynamic (2D MHD) simulations  
 28 were compared with two of the observed MMS events. Comparison of the observations  
 29 with the 2D MHD simulations indicates that the new region sorting method is reliable  
 30 and robust. The ability to automatically detect separate plasma regions on either side  
 31 of a moving boundary and determine the KHI growth rate may prove useful for future  
 32 work identifying and studying secondary processes associated with the KHI.

## 33 **1 Introduction**

34 The ways in which the solar wind (SW) couples to the Earth’s magnetosphere and  
 35 its impacts on local space weather is a fundamental question of space physics. Several  
 36 mechanisms operating at the magnetopause boundary, such as magnetic reconnection  
 37 [*Paschmann et al.*, 1979; *Sonnerup et al.*, 1981; *Gosling et al.*, 1986; *Burch and Phan*,  
 38 2016] and viscous interactions [*Axford and Hines*, 1961; *Otto and Fairfield*, 2000; *Fair-*  
 39 *field et al.*, 2000], are responsible for the transfer of mass and energy from the solar wind  
 40 to the magnetosphere. Understanding the detailed effects of these processes is vital to  
 41 predict and help prevent negative outcomes from space weather. Consider as an exam-  
 42 ple, the dawn-dusk asymmetry of the magnetosphere plasma sheet.

43 Observations from Defense Meteorological Satellite Program (DMSP) and Time  
 44 History of Events and Macroscale Interactions during Substorm (THEMIS) spacecraft  
 45 have established that the cold component ions of the plasma sheet are 30-40% hotter in

46 the dawn flank than in the dusk [Hasegawa *et al.*, 2003; Wing *et al.*, 2005]. Dimmock *et al.*  
 47 [2015] conducted a statistical study of the magnetosheath source population as observed  
 48 by THEMIS spacecraft over seven years, which showed ions in the dawn flank are on av-  
 49 erage 10-15% hotter than those in the dusk flank. This asymmetry is more pronounced  
 50 under fast ( $> 400$  km/s) SW conditions [Dimmock *et al.*, 2015]. However, even during  
 51 fast SW, the asymmetry of the magnetosheath source plasma is insufficient to produce  
 52 the observed asymmetry in the plasma sheet. MHD simulations were unable to repro-  
 53 duce the observed sheath asymmetry, but it was apparent in hybrid models, suggesting  
 54 a kinetic scale mechanism is responsible for asymmetrically driving the heating of cold  
 55 component ions in the sheath [Dimmock *et al.*, 2015].

56 Several physical mechanisms have been proposed as drivers of the observed plasma  
 57 sheet asymmetry. The Kelvin-Helmholtz instability (KHI), which occurs regularly at the  
 58 magnetopause boundary, is one such mechanism [Otto and Fairfield, 2000; Fairfield *et al.*,  
 59 2000; Nykyri *et al.*, 2003; Hasegawa *et al.*, 2004; Nykyri *et al.*, 2006; Taylor *et al.*, 2008;  
 60 Foullon *et al.*, 2008; Merkin *et al.*, 2013; Lin *et al.*, 2014; Ma *et al.*, 2014a,b; Nykyri *et al.*,  
 61 2017; Ma *et al.*, 2017; Sorathia *et al.*, 2019]. The KHI occurs in regions of large shear  
 62 flow [Chandrasekhar, 1961], such as the boundary between the shocked SW (the mag-  
 63 netosheath) and the relatively stagnant magnetosphere [Miura and Pritchett, 1982]. Long  
 64 established as a source for momentum and energy transport from the SW to the mag-  
 65 netosphere [Miura, 1984, 1987], later simulations and observations have shown non-linear  
 66 stages of the KHI are also capable of reconnection and mass transport [Nykyri and Otto,  
 67 2001, 2004; Nykyri *et al.*, 2006; Hasegawa *et al.*, 2009] and ion heating via kinetic wave  
 68 modes within the vortex [Moore *et al.*, 2016, 2017]. Compressional waves, like Kelvin-  
 69 Helmholtz or ultra-low frequency (ULF) waves, can also lead to kinetic Alfvén wave (KAW)  
 70 generation via mode conversion [Johnson *et al.*, 2001; Chaston *et al.*, 2007]. Recent work  
 71 by Nykyri *et al.* [2021] has suggested that KAWs associated with the KHI can contribute  
 72 to parallel electron heating, but in that case, were insufficient to account for the total  
 73 observed electron heating. Identifying the detailed mechanism or mechanisms driving  
 74 electron scale waves within the KHI and quantifying their contribution to electron heat-  
 75 ing is still an open question.

76 Observations have shown the KHI may form on both the dawn and dusk flanks un-  
 77 der any orientation of the interplanetary magnetic field (IMF) [Kavosi and Reader, 2015],  
 78 but simulations have shown a preference for dawn flank formation when the IMF is in

79 a Parker Spiral (PS) orientation [*Nykyri, 2013; Adamson et al., 2016*]. Work by *Henry*  
 80 *et al.* [2017] analyzed the events presented in *Kavosi and Reader* [2015] and confirmed  
 81 this preference observationally. *Henry et al.* [2017] also confirmed a preference for KHI  
 82 formation at the dusk flank for high solar wind speeds under northward IMF (NIMF).  
 83 As PS is the most statistically common IMF orientation, it follows that the associated  
 84 preference for dawn-side KHI development would also be statistically more common. Such  
 85 asymmetry in the formation of KHI, combined with Kelvin-Helmholtz (KH) driven sec-  
 86 ondary processes like reconnection and kinetic scale waves, make the KHI a strong can-  
 87 didate to drive the dawn-dusk asymmetry of cold-component ions in the plasma sheet.

88 The launch of the Magnetospheric Multiscale (MMS) satellites presents a new op-  
 89 portunity to extend this study of the KHI and its associated secondary processes to smaller  
 90 scales with higher resolution measurements. Within months of its launch, MMS had en-  
 91 countered KHI [*Eriksson et al., 2016*]. The event reported by *Eriksson et al.* [2016] has  
 92 been the subject of several case studies: *Li et al.* [2016] found evidence of Alfvénic ion  
 93 jets and electron mixing due to reconnection at the trailing edge of the vortex; *Wilder*  
 94 *et al.* [2016] noted compressed current sheets and evidence of ion-acoustic waves, and *Stawarz*  
 95 *et al.* [2016] took advantage of MMS’s high temporal and spatial resolutions to study tur-  
 96 bulence generated by the KHI. These secondary processes would contribute to ion heat-  
 97 ing and plasma transfer across the magnetopause boundary.

98 Case studies are useful in identifying the fine-scale secondary processes associated  
 99 with the KHI, but statistical studies are necessary to fully understand their role and quan-  
 100 tify their contribution to heating and driving the plasma sheet asymmetry. It is there-  
 101 fore imperative, as a first step, to build a database of MMS encounters with KHI. Com-  
 102 parison of the location, duration, and prevailing IMF conditions of many events with the  
 103 growth rates and unstable solid angles can help establish patterns which may prove in-  
 104 formative in understanding the role KHI plays in magnetospheric dynamics (e.g., in gen-  
 105 erating dawn-dusk asymmetries via secondary, “cross-scale” processes or affecting the  
 106 radiation belt electron populations via ULF wave generation or magnetopause shadow-  
 107 ing).

108 In this paper we present a list of MMS encounters with the KHI and the physical  
 109 characteristics of each, which may be used for future studies of small scale secondary pro-  
 110 cesses. The MMS instrumentation and observational signatures used to identify the KHI

111 encounters are described in Section 2.1 and 2.2, respectively. Growth rates and the un-  
 112 stable solid angle used to characterize the KHI are derived in Section 2.3 . Section 2.4  
 113 details the methodology used to separate magnetosheath and magnetospheric regions of  
 114 the observed events, in order to calculate the growth rates and unstable solid angle for  
 115 each event. Results of these calculations are presented in Section 3. The methodology  
 116 was also tested using 2-dimensional magnetohydrodynamic simulations as described in  
 117 Section 4. Conclusions are presented and discussed in Section 5.

## 118 **2 Methodology**

### 119 **2.1 MMS Instrumentation**

120 Observational data reported here is level 2 survey data from MMS1 [*Burch et al.*,  
 121 2016]. Spacecraft separations are at most 230 km, and most often between 20 and 50 km,  
 122 well below the typical size of the KHI, thus all spacecraft are expected to observe the  
 123 same signatures and a single craft is sufficient to identify the KHI. Ion energy spectra  
 124 and ion and electron moments are taken from the Fast Plasma Investigation (FPI) [*Pol-  
 125 lock et al.*, 2016]. The Flux Gate Magnetometer (FGM) provides the DC magnetic field  
 126 [*Russell et al.*, 2016; *Torbert et al.*, 2016]. Data file versions used are v3.3.0.cdf for FPI  
 127 and v4.18.0.cdf for FGM. SW data are taken from the OMNI database [*King and Pa-  
 128 pitashvili*, 2005].

### 129 **2.2 Observational Signatures & Identification of the KHI**

130 Between September 2015 and March 2020, MMS made thousands of full and par-  
 131 tial crossings of the magnetopause. In order to narrow the search field, we limited our-  
 132 selves to magnetopause crossings which were noted to be unstable in the MMS event database.  
 133 Approximately 100 unique intervals were tagged as potentially containing KHI activity.  
 134 These crossings were checked by eye to determine if they exhibited the characteristics  
 135 of the KHI. These characteristic signatures are as follows:

- 136 • Quasi-periodic fluctuations in omnidirectional ion energy;

137 When MMS crosses a stable magnetopause boundary, we expect to see a smooth tran-  
 138 sition from plasma with energy typical of the magnetosheath to plasma with typical mag-  
 139 netospheric energy (or vice versa). When the boundary is not stable, this transition will

140 not be smooth, and may show alternating regions of plasma with energies typical of the  
 141 magnetosheath and magnetosphere, as well as mixed energies due to plasma mixing in  
 142 the KH vortex. For the case of a boundary disturbed by a periodic instability like the  
 143 KHI, these alternating regions should also be relatively periodic.

- 144 • Quasi-periodic, anti-correlated fluctuations in ion density and temperature;

145 The periodic observation of the magnetosheath and magnetospheric regions will also be  
 146 evident in the ion density and temperature, as MMS alternately encounters regions of  
 147 plasma from the cold, dense magnetosheath and the hot, tenuous magnetosphere.

- 148 • Velocity shear(s) on the order of 100s of km/s;

149 Large velocity shears are common at the flank magnetopause, where the magnetosphere  
 150 is relatively stagnant and the magnetosheath plasma is accelerating from low speeds im-  
 151 mediately after the shock to “catch up” with the SW speed further downtail [*Dimmock*  
 152 *and Nykyri, 2013*]. Large velocity shears are also a necessary condition for the develop-  
 153 ment of the KHI [*Chandrasekhar, 1961; Miura, 1984, 1987*].

- 154 • Fluctuations in the total magnetic field;

155 The total strength of the magnetic field will vary as the KH vortex compresses the field  
 156 lines.

- 157 • Bipolar variations in the normal component of the magnetic field

158 Fluctuations in the magnetic field should appear as bipolar variations in the normal com-  
 159 ponent as the vortex twists the field lines. Changes in the normal component and to-  
 160 tal magnetic field help distinguish the KHI from a shifting boundary, such as a response  
 161 to SW dynamic pressure variations.

- 162 • Fluctuations in total pressure, specifically decreases corresponding to the center  
 163 of the KH vortex, where  $B_N$  is near 0.

164 The rotational nature of the KHI creates an outward force which is balanced by a pres-  
 165 sure gradient, resulting in a decrease of total pressure at the center of the vortex. KHI  
 166 events thus show a lower total pressure near the center of the vortex (where  $B_N$  is zero)

167 and higher pressure in the spine region. This signature allows us to distinguish the KHI  
 168 from a flux transfer event (FTE) in which total pressure typically increases when  $B_N$   
 169 is zero [Nykyri *et al.*, 2006; Zhao *et al.*, 2016]. We note that MMS will not always ob-  
 170 serve this particular signature, depending on the path MMS takes through the instabil-  
 171 ity.

172 Twisting at the boundary is also evident in a comparison of the normal component  
 173 with the total bulk velocity. At a quiet boundary, plasma bulk velocity is generally tan-  
 174 gential to the boundary. As a KHI twists the boundary, the normal component of the  
 175 velocity increases. We compare the maximum absolute value of the normal velocity com-  
 176 ponent to the total velocity at the time of observation. For a well developed vortex, the  
 177 maximum value of the normal velocity should be a significant fraction of the total ve-  
 178 locity. The ratio of the maximum normal velocity to the total velocity for each event is  
 179 presented in Section 3

180 To obtain the normal component of the field, observed magnetic field data is ro-  
 181 tated into boundary normal (LMN) coordinates using the maximum variance of the elec-  
 182 tric field (MVA-E) technique. The general method for variance analysis techniques is given  
 183 in *Sonnerup and Scheible* [1998]. *Nykyri et al.* [2011a,b] showed the single spacecraft MVA-  
 184 E technique is sufficient for identification of the boundary normal direction when the plasma  
 185 bulk velocity and magnetic field are primarily tangential to the boundary, as is typically  
 186 the case during KHI. It is also used here, rather than a multi-spacecraft method, to al-  
 187 low for automation of the analysis. For MVA-E, the direction in which the convective  
 188 ( $\mathbf{v} \times \mathbf{B}$ ) electric field variance is maximized (i.e., the direction of the maximum eigen-  
 189 vector of the variance matrix) is taken as the normal direction,  $\mathbf{N}$ . The 180° ambigu-  
 190 ity in the normal direction is resolved by requiring the unit normal be positive pointing  
 191 outward from the magnetosphere. Tangential directions,  $\mathbf{L}$  and  $\mathbf{M}$ , are defined by the  
 192 intermediate and minimum eigenvectors of the MVA-E matrix, but are not relevant to  
 193 the current analysis.

194 All of the above signatures are present in the two example cases shown in Figures  
 195 1 and 2. The first five signatures are present in all identified events listed in Table 1. The  
 196 final signature is dependent on the MMS trajectory through the KHI, and may or may  
 197 not be visible in the observational data for any given event.

198 Figure 1 shows MMS1 survey level observations from 06:00 to 07:00 UT on 15 Oc-  
 199 tober 2015, the availability of burst mode data for portions of the interval is indicated  
 200 with a blue bar at the top of the figure. MMS passed through the dusk flank of the day-  
 201 side magnetopause during strongly duskward IMF. The omni-directional ion energy spec-  
 202 trogram in panel (a) shows the expected quasi-periodic variations throughout the inter-  
 203 val, which are well matched by anti-correlated changes in ion density and temperature  
 204 (c). A velocity shear on the order of 200 km/s is visible near 06:26 UT in panel (d). The  
 205 GSM magnetic field in panel (e) shows 20-40nT fluctuations characteristic of the KHI  
 206 from 06:26 to 06:39 UT and again near from 06:48 to 06:55 UT. These fluctuations are  
 207 also present as bipolar variations in the normal component of the magnetic field (f). De-  
 208 creases in total pressure (g) are visible starting around 06:27 UT and continuing through  
 209 06:48 UT. The decreases of total pressure correspond with times at which the normal  
 210 magnetic field component is near 0, particularly from 06:35-06:40 UT.

217 Survey mode MMS1 observations of another KHI encounter from 16:35 to 19:07  
 218 UT on 26 September 2017 are shown in Figure 2. The blue bar at top again indicates  
 219 burst mode data is available for portions of the interval. MMS crossed the dusk flank  
 220 tail magnetopause while the IMF was in a PS orientation with a strong northward com-  
 221 ponent. Quasi-periodic fluctuations in omni directional ion spectra are observable through-  
 222 out the interval in panel (a) and are accompanied by anti-correlated variations in ion den-  
 223 sity and temperature (c). Velocity shears (d) on the order of 200 km/s occur regularly  
 224 throughout the interval. Panel (e) shows fluctuations around 10 nT in the total mag-  
 225 netic field, which are also visible as bipolar signatures in the normal component of the  
 226 magnetic field (f). Decreases in total pressure (g) of approximately 0.1 nPa correspond  
 227 well with times when BN is near 0.

232 Table 1 summarizes the 45 MMS encounters with the KHI between September 2015  
 233 and March 2020. In this time period MMS observed more KH events on the dusk side  
 234 magnetopause (29) than on the dawn-side (16). Events are evenly distributed between  
 235 the dayside and tail magnetopause: 22(23) events occur sunward(tailward) of the ter-  
 236 minator. KHI in the tail are all observed in or after May 2017, which is primarily due  
 237 to a sampling effect of the MMS orbit change from Phase One, which targeted the day-  
 238 side magnetopause, to Phase Two, which targeted the tail. The observed events ranged  
 239 in duration from as little as 10 minutes to nearly 13 hours. Burst mode data is available

240 for portions of all 45 events, which will be useful for future studies of smaller scale pro-  
 241 cesses within the KHI.

242 SW data from OMNI is available for 44 of the 45 events, which occur under a va-  
 243 riety of IMF orientations and solar wind conditions. We consider the planar and  $B_Z$  com-  
 244 ponents separately. At the time at which MMS first observes the KHI, the planar com-  
 245 ponents of the IMF show a preference for PS (17). Less common are radial, duskward,  
 246 dawnward (8 each), and ortho-Parker Spiral (OPS) (3) orientations. For the duration  
 247 of each event, the planar components of the average IMF configurations show a prefer-  
 248 ence for the PS orientation (17), followed by radial and dawnward (8 each) orientation.  
 249 Duskward (6) and OPS (5) orientations are less common. At event onset, the  $\mathbf{B}_Z$  com-  
 250 ponent of the IMF was more often northward (27) than southward (17). This preference  
 251 for NIMF orientation holds true for the duration of each event: 26 (18) of the events oc-  
 252 curred under average  $\mathbf{B}_Z$  positive (negative). The IMF vectors and values of the SW con-  
 253 ditions for each event are available in the Supplement. SW parameters are discussed and  
 254 correlated with KHI growth rates in Section 3.

255 Having identified MMS encounters with the KHI, we next calculate the growth rate  
 256 and unstable solid angle of each event and compare the results with the prevailing so-  
 257 lar wind and IMF properties.

### 258 2.3 Instability Growth Rate & Unstable Solid Angle

259 Assuming an infinitely thin boundary layer, a region unstable to the KHI will sat-  
 260 isfy the KH instability criteria

$$[\mathbf{k} \cdot (\mathbf{v}_1 - \mathbf{v}_2)]^2 \geq \frac{n_1 + n_2}{4\pi m_0 n_1 n_2} [(\mathbf{k} \cdot \mathbf{B}_1)^2 + (\mathbf{k} \cdot \mathbf{B}_2)^2] \quad (1)$$

261 where  $\mathbf{v}_i$ ,  $n_i$ , and  $\mathbf{B}_i$  are the the velocity, density, and magnetic field on either side of  
 262 the velocity shear layer and  $\mathbf{k}$  is the wave vector [*Chandrasekhar, 1961*].

263 Equation 1 may be rearranged to determine the normalized growth rate of the KHI  
 264 in a particular region, which is defined as

$$Q/k = \sqrt{a_1 a_2 (\Delta \mathbf{v} \cdot \hat{\mathbf{k}})^2 - a_1 (\mathbf{v}_{A1} \cdot \hat{\mathbf{k}})^2 - a_2 (\mathbf{v}_{A2} \cdot \hat{\mathbf{k}})^2} \quad (2)$$

265 where  $a_i$  is a density parameter for either side of the boundary, defined by  $a_i = \rho_i / (\rho_1 +$   
 266  $\rho_2)$ ,  $\mathbf{v}_{A1}$  is the Alfvén velocity, and  $\hat{\mathbf{k}}$  is the unit wave vector (thus the growth rate is nor-  
 267 malized to the wavelength), pointing in the direction of maximum growth. We use only

**Table 1.** The date, onset time, duration, GSM location, and estimated wavelength of 45 KHI events observed by MMS from September 2015 to March 2020.

Burst mode data is available for portions of all events.

Event Number, Date	Onset Time [UT]	Duration [min]	GSM Location [ $R_E$ ]	KH Wave-length [ $R_E$ ]	Event Number, Date	Onset Time [UT]	Duration [min]	GSM Location [ $R_E$ ]	KH Wave-length [ $R_E$ ]
01, 08-Sep-15	09:00	170	[5.0, 7.4, -4.5]	2.80	24, 19 May-17	23:58	107	[-17.8, -16.6, -2.1]	20.72
02, 15-Sep-15	10:45	240	[5.1, 8.7, -5.5]	5.00	25, 20 May-17	02:00	150	[-17.6, -17.4, -0.6]	26.65
03, 11-Oct-15	10:30	30	[8.7, 6.5, -4.7]	3.71	26, 20 Sep-17	22:32	43	[-10.8, 20.9, 1.3]	8.20
04, 15-Oct-15	06:00	60	[9.0, 4.1, -2.3]	2.29	27, 26 Sep-17	16:35	152	[-9.3, 19.6, -0.9]	6.47
05, 17-Oct-15	16:00	28	[6.4, 7.8, -4.1]	4.94	28, 16 Oct-17	14:30	50	[-4.0, 18.6, -2.7]	7.71
06, 18-Oct-15	15:00	25	[7.2, 7.5, -4.4]	8.18	29, 30 Oct-17	19:05	35	[-0.6, 17.3, 1.6]	4.20
07, 22-Dec-15	22:15	35	[7.9, -5.7, -1.8]	2.58	30, 02 Nov-17	17:25	50	[-0.9, 14.8, 0.8]	6.38
08, 11-Jan-16	20:52	18	[6.2, -7.6, -3.4]	1.99	31, 03 May-18	00:15	35	[-9.3, -17.5, -2.3]	8.43
09, 19-Jan-16	19:57	38	[5.3, -8.2, -3.9]	3.25	32, 18 Sep-18	15:50	25	[-14.1, 20.6, -1.0]	5.17
10, 05-Feb-16	18:55	35	[3.3, -9.3, -5.0]	5.97	33, 24 Sep-18	14:10	195	[-14.1, 20.3, -1.6]	19.35
11, 07-Feb-16	03:45	55	[7.0, -6.9, -3.5]	4.20	34, 02 Oct-18	23:45	35	[-10.8, 22.5, 2.1]	11.25
12, 18-Feb-16	19:30	70	[2.5, -9.7, -6.3]	6.81	35, 04 Oct-18	17:25	10	[-0.8, 16.2, -0.2]	2.50
13, 25-Feb-16	18:55	70	[1.3, -9.9, -6.5]	2.26	36, 13 Apr-19	07:45	30	[-0.6, -17.5, 2.4]	9.68
14, 26-Sep-16	14:15	70	[2.7, 8.5, -5.4]	11.85	37, 03 Jun-19	23:05	75	[-2.2, -14.9, -3.8]	7.46
15, 27-Sep-16	19:50	20	[0.3, 11.5, -3.4]	2.62	38, 25 Sep-19	13:45	765	[-16.7, 22.0, -0.2]	12.33
16, 04-Oct-16	18:20	70	[1.8, 11.2, -3.6]	9.51	39, 02 Oct-19	08:15	165	[-9.9, 21.5, -4.5]	8.54
17, 10-Oct-16	14:40	60	[4.3, 9.3, -5.0]	9.43	40, 02 Oct-19	16:00	80	[-12.9, 23.5, -2.1]	13.03
18, 24-Oct-16	10:50	30	[6.8, 6.1, -4.3]	1.09	41, 02 Oct-19	21:40	25	[-14.6, 24.0, 1.1]	7.11
19, 04-Nov-16	11:45	75	[8.1, 7.2, -3.8]	2.28	42, 06 Oct-19	14:50	175	[-14.8, 24.4, -4.2]	17.10
20, 03-May-17	02:00	150	[-12.9, -19.7, -3.9]	17.39	43, 15 Oct-19	19:00	75	[1.2, 12.8, 2.9]	8.81
21, 08-May-17	13:00	110	[-14.8, -17.2, 0.3]	11.50	44, 22 Oct-19	22:00	20	[1.8, 15.3, 3.8]	3.76
22, 11-May-17	12:00	150	[-15.6, -18.2, 1.4]	18.47	45, 12 Nov-19	20:30	75	[6.7, 11.8, 5.2]	7.04
23, 11-May-17	15:44	31	[-15.3, -19.2, -0.3]	7.75					

268 proton data to determine the values in Equation 2 as the low mass electrons have no mean-  
 269 ingful influence on the growth rate, and minor ion species are not abundant enough to  
 270 contribute significantly.

271 Note Equation 2 is an upper limit of the growth rate for an observed event due to  
 272 the assumption of an infinitely thin boundary, which is not true for the magnetopause.  
 273 Equations 1 and 2 also assume an incompressible plasma, yet for very high ( $> 600$  km/s)  
 274 SW speeds, the compressibility is generally sufficient to stabilize the development of the  
 275 KHI. Due to these assumptions, the growth rate as determined by Equation 2 is an over-  
 276 estimate of the growth rate for an observed KHI. It must also be noted that MMS is un-  
 277 likely to observe the source region of the KHI and local conditions may not match those  
 278 of the source region. The difference in growth rate from the source region to the obser-  
 279 vation point is not predictable from observations.

280 In order to compare the growth rates for KHI events observed at various locations  
 281 and under a variety of SW and IMF conditions, we make it unitless via normalization  
 282 to the local fast mode speed,  $v_{fm} = \sqrt{v_A^2 + c_s^2}$ . Both magnetic tension and compress-  
 283 ibility have stabilizing effects on the KHI. Likewise, the fast mode speed is dependent  
 284 on magnetic tension via the Alfvén velocity,  $v_A$ , and compressibility via the sound speed,  
 285  $c_s$ . Further, *Miura and Pritchett* [1982] showed the KHI growth rate is strongly corre-  
 286 lated to the fast mode speed, and is stable for  $Q/k > v_{fm}$ , thus it is more physically  
 287 meaningful to normalize to the fast mode speed than another characteristic speed.

288 It is also important to note, our expression of the fast mode speed here is an up-  
 289 per limit which assumes the magnetic field is perpendicular to the bulk velocity. When  
 290 the field and velocity are parallel, the larger of the sound or Alfvén speed is used as the  
 291 fast mode speed. This means the unitless growth rate we present is a lower bound, and  
 292 may be larger depending upon the relative geometry of the magnetic field and bulk ve-  
 293 locity.

The fast mode speed is not equal in the magnetosheath (sub-index *msh*) and mag-  
 netosphere (sub-index *msh*), so we normalize to the mean of the two, such that

$$Q_{unitless} = \frac{Q/k}{v_{fm}}$$

294 where  $v_{fm} = \frac{1}{2}(v_{fmmsh} + v_{fmmsh})$ .

295 In Equation 2 the direction of  $\hat{\mathbf{k}}$  is chosen to maximize the normalized growth rate,  
 296 but many directions of  $\hat{\mathbf{k}}$  may satisfy the instability criteria. This range of angles capa-  
 297 ble of satisfying the instability criteria can be used to determine just how susceptible a  
 298 region is to the development of the KHI.

299 The KHI may propagate in any direction  $\hat{\mathbf{k}}$  for which  $Q/k$  is real (the right hand  
 300 side of Equation 2 is positive under the square root). If we express  $\hat{\mathbf{k}}$  in terms of the spher-  
 301 ical angles  $\phi$  and  $\theta$ , the percent of the  $4\pi$  solid angle that satisfies the KHI instability  
 302 criteria at a given location may be calculated. We term this percentage the “unstable  
 303 solid angle” [*Burkholder et al.*, 2020; *Nykyri et al.*, 2021]. Events with larger unstable  
 304 solid angles are likely to be KHI.

305 Growth rate alone is not a sufficient parameter to characterize the KHI; cases with  
 306 small growth rates can be indicative of a source region further upstream, such that the  
 307 KHI has already created a more diffuse boundary layer. The KHI is a convective insta-  
 308 bility which dissipates stored energy as it develops, thus growth rate and the unstable  
 309 solid angle are maximized just prior to the formation of the KH vortex. The nature of  
 310 in-situ observations, however, dictates we cannot identify a KHI until it is relatively well  
 311 developed. Thus small growth rates and unstable solid angles are not necessarily counter-  
 312 indicative of the presence of the KHI, but may instead be features of later stage KH waves.

313 As a secondary check for events with low growth rates, we plot tailward velocity  
 314 as a function of density to see if the KHI vortex had rolled over, examples of which are  
 315 seen in Figure 3. As the KHI develops, it may form non-linear vortices in which low den-  
 316 sity magnetospheric plasma becomes trapped and is dragged tailward with magnetosheath-  
 317 like velocities. This is seen in observations as low density plasma (typically associated  
 318 with the magnetosphere) flowing tailward with the magnetosheath [*Hasegawa et al.*, 2006;  
 319 *Taylor et al.*, 2012], and is apparent as points in the lower left quadrant of Figure 3. For  
 320 the 15 October 2015 event, ions do not show signatures of roll-over, indicating the KHI  
 321 is in an earlier phase of development. For the 26 September 2017 event, ions with magnetosphere-  
 322 like density flowing with magnetosheath-like velocities are present, indicating the KHI  
 323 has rolled over to form a well-developed vortex.

331 Another indicator of vortex roll-over within the KHI is a comparison of the nor-  
 332 mal component with the total bulk velocity. At a quiet boundary, plasma bulk veloc-  
 333 ity is generally tangential to the boundary. As a KHI twists the boundary, the normal

334 component of the velocity increases. We compare the maximum absolute value of the  
 335 normal velocity component to the total velocity at the time of observation. For a well  
 336 developed vortex, the maximum value of the normal velocity should be a significant frac-  
 337 tion of the total velocity.

338 Results for the growth rate, unitless growth rate, unstable solid angle, and relative  
 339 value of normal velocity are presented in Section 3.

## 340 2.4 Automated Region Sorting

341 Calculation of the growth rate and unstable solid angle requires the identification  
 342 of separate regions of magnetosheath and magnetospheric plasma on either side of the  
 343 magnetopause boundary. This is made difficult by the plasma mixing inherent within  
 344 KH waves. In case studies it is common to select a few minutes of data in the pure mag-  
 345 netosheath and magnetosphere regions well away from the unstable boundary area. This  
 346 is not, however, the most robust or efficient way to handle region identification for the  
 347 many cases necessary for a statistical study. Instead, we seek to automate the process  
 348 of separating the magnetosheath and magnetosphere regions.

349 The unperturbed flank magnetosheath is characterized by cold, dense plasma flow-  
 350 ing tailward at high speeds with the shocked SW. In contrast the magnetospheric plasma  
 351 near the flanks is hot, tenuous, and relatively stagnant. Thus, a combination of density,  
 352 temperature, and the  $X$ -component of the bulk velocity may be used to separate data  
 353 from the magnetosheath and magnetosphere regions. The isolated data provides the mean  
 354 values of density, velocity, etc. in each region which are used in the calculation of the  
 355 growth rates and unstable solid angle.

356 The magnetosheath is identified by the product of ion density and tailward veloc-  
 357 ity divided by the average ion temperature,  $nv_{tail}/T$ . The GSM- $X$  velocity component,  
 358  $v_X$ , is measured to be large and negative in the sheath and small, either positive or neg-  
 359 ative, in the magnetosphere. To simplify our parameter, we shift the tailward velocity  
 360 to be strictly positive with a minimum value at 0, such that  $v_{tail} = |v_X - \max(v_X)|$ .  
 361 The resulting parameter,  $nv_{tail}/T$ , is thus large in the magnetosheath and small in the  
 362 magnetosphere. We identify the sheath as any region in which the value of  $nv_{tail}/T$  is  
 363 greater than 1.5 times the magnetopause value. The magnetopause value is defined as  
 364 the mean of the largest 12.5% and smallest 12.5% of all  $nv_{tail}/T$  values (for a total of

365 25% of available data) for each event. This method allows us to reliably identify the mag-  
 366 netosheath regions near the KHI while avoiding the inclusion of mixed and transition  
 367 regions in our calculations of the KHI growth rate and unstable solid angle (see the Sup-  
 368plementary Information for details justifying the data ranges and cutoff values presented  
 369 here).

370 The  $nv_{tail}/T$  parameter does not, however, reliably isolate magnetospheric plasma.  
 371 Instead, we use the ion specific entropy,  $S = T/n^{2/3}$ , to identify magnetospheric regions  
 372 within each KHI event. The hot, tenuous magnetosphere has much higher specific en-  
 373 tropy than the magnetosheath, so we may follow the same procedure as employed for  
 374 isolating the magnetosheath with specific entropy in place of the  $nv_{tail}/T$  parameter to  
 375 separate the magnetosphere. That is, any region with specific entropy 1.5 times greater  
 376 than the magnetopause value is considered to be the magnetosphere. Again the mag-  
 377netopause value is the mean of the largest 12.5% and smallest 12.5% (25% total) of all  
 378 entropy values for the event. This allows for reliable determination of the magnetospheric  
 379 regions near the KHI without including mixed and transition plasma regions (see Sup-  
 380plementary Information).

381 The results of this region sorting method are depicted in panel b of Figures 1  
 382 and 2. Red (blue) bars represent regions of magnetosphere (magnetosheath) plasma. The  
 383 green bar identifies regions of mixed plasma. In both example events, the identified re-  
 384 gions are in good agreement with omnidirectional ion energy spectrograms and the ion  
 385 density and temperature measurements. In Figure 3 red and blue points also represent  
 386 the magnetosphere and magnetosheath respectively. In the 2017 case, rolled-over plasma  
 387 is considered mixed, despite having density more characteristic of the magnetosphere.  
 388 This is a good indicator that our method of automatically separating regions is select-  
 389 ing only pure magnetosheath and magnetospheric plasmas and excluding regions where  
 390 the KHI has already caused mixing.

391 Having isolated the separate regions, we then calculate mean values of density, tem-  
 392 perature, velocity, and magnetic field on either side of the boundary. These values are  
 393 checked to ensure they fall within typical ranges for the magnetosheath and magneto-  
 394 sphere before they are used in calculation of the growth rate and unstable solid angle.  
 395 The new method was also tested using simulation data, and provided good agreement  
 396 with known values (see Section 4 and Supplementary Information).

### 3 Observational Results

Having separated the magnetosheath and magnetospheric regions of each event, growth rates (GR), unitless growth rates (UGR), and unstable solid angles (USA) are calculated. Results for all 45 events are listed in Table 2. GR range from 3.93 to 103.16 km/s. When normalized to the fast mode speed, UGR range from 0.005 to 0.325, but more typically are between 0.010 and 0.200. That is, the KHI typically develops at 1-20% of the local fast mode speed; only 1 event falls below this range and 7 above it. USA range from 0.06 to 39.51. At its maximum, the normal component of velocity often accounts for more than 60%, and occasionally all, of the total velocity, indicating the observed KH waves have significantly twisted the boundary. Events with strongly twisted boundaries are good candidates for future studies of reconnection and other secondary processes driven by the KHI.

GR, UGR, and USA show some dependence on location, as can be seen in Figure 4. The locations of the KHI events observed by MMS are plotted in the GSM X-Y (left column), X-Z (middle column), and Y-Z (right column) planes and color coded according to the GR (top row), UGR (middle row), and USA (bottom row). KHI observed near the sub-solar point tend to have lower GR than those observed further along the magnetopause, particularly those observed along the tail. This is still apparent even when growth rates are normalized to the local fast mode speeds. This is likely due to the low velocity shear near the subsolar point. Immediately after the bow shock, the magnetosheath plasma is slowed significantly from SW speeds, and the shear between the sheath and magnetosphere is much lower than further downtail, where the magnetosheath plasma has accelerated and returned to values of SW velocity. The low velocity shear near the subsolar point will result in lower GR and UGR, as can be seen from Equation 2.

USA shows a similar pattern as the GR and UGR, with larger values observed further down tail. Again, this can be explained by the large velocity shears encountered along the tail magnetopause. On the dayside, the shocked solar wind of the magnetosheath is still accelerating back up to SW speed after encountering the obstacle of earth's magnetosphere and bow shock, thus velocity shears between the sheath and magnetosphere are smaller. Further down tail, the magnetosheath plasma has re-achieved the high SW flow speed, thus increasing the shear between the two regions. For larger velocity shears,

409 **Table 2.** Growth rates (GR), unitless growth rates (UGR), unstable solid angles (USA), and  
 410 the relative value of the maximum normal velocity component for each of the 45 KHI events  
 411 observed by MMS from September 2015 to March 2020. At its maximum, the normal velocity  
 412 component is a significant fraction of the total velocity for most events. The asterisk indicates  
 413 the high-latitude event studied by *Nykyri et al.* [2021] and *Michael et al.* [2021]

Event Number, Date	GR [km/s]	UGR	USA [%]	$v_{Nmax}$ / $v_{tot}$	Event Number, Date	GR [km/s]	UGR	USA [%]	$v_{Nmax}$ / $v_{tot}$
01, 08-Sep-15	81.63	0.081	6.37	0.96	24, 19-May-17	90.54	0.186	29.00	0.93
02, 15-Sep-15	16.27	0.019	0.82	0.99	25, 20-May-17	47.42	0.066	30.22	0.75
03, 11-Oct-15	15.68	0.016	0.42	0.58	26, 20-Sep-17	53.99	0.145	18.75	0.19
04, 15-Oct-15	8.83	0.007	0.11	0.85	27, 26-Sep-17	52.01	0.189	24.23	0.83
05, 17-Oct-15	25.05	0.032	4.01	0.92	28, 16-Oct-17	26.03	0.047	6.74	0.79
06, 18-Oct-15	52.31	0.063	9.07	0.83	29, 30-Oct-17	11.51	0.023	4.70	0.97
07, 22-Dec-15	10.41	0.010	0.29	0.83	30, 02-Nov-17	39.55	0.109	5.95	0.67
08, 11-Jan-16	17.47	0.015	0.27	0.89	31, 03-May-18	95.59	0.325	23.37	0.97
09, 19-Jan-16	13.78	0.025	0.12	0.52	32, 18-Sep-18	40.87	0.090	9.96	0.91
10, 05-Feb-16	22.31	0.028	5.74	0.93	33, 24-Sep-18	71.16	0.227	36.91	0.73
11, 07-Feb-16	13.36	0.019	0.16	0.66	34, 02-Oct-18	41.17	0.111	10.18	0.65
12, 18-Feb-16	34.90	0.038	8.96	1.00	35, 04-Oct-18	31.26	0.081	6.16	0.50
13, 25-Feb-16*	5.01	0.012	0.08	0.69	36, 13-Apr-19	48.93	0.089	15.66	0.76
14, 26-Sep-16	51.46	0.068	7.26	0.99	37, 03-Jun-19	42.25	0.108	16.63	0.94
15, 27-Sep-16	84.07	0.117	8.37	0.96	38, 25-Sep-19	74.22	0.198	28.04	0.91
16, 04-Oct-16	54.67	0.063	7.17	0.70	39, 02-Oct-19	29.28	0.083	6.10	0.58
17, 10-Oct-16	43.30	0.059	8.98	0.75	40, 02-Oct-19	96.46	0.209	26.71	0.82
18, 24-Oct-16	3.93	0.005	0.06	0.71	41, 02-Oct-19	37.12	0.111	18.09	0.52
19, 04-Nov-16	16.78	0.019	0.78	0.95	42, 06-Oct-19	82.43	0.210	34.49	0.98
20, 03-May-17	56.65	0.197	39.51	0.85	43, 15-Oct-19	94.08	0.296	18.37	0.98
21, 08-May-17	84.15	0.278	29.87	1.00	44, 22-Oct-19	52.52	0.110	12.00	1.00
22, 11-May-17	45.56	0.103	12.07	0.87	45, 12-Nov-19	103.16	0.250	14.34	0.90
23, 11-May-17	49.99	0.198	13.33	0.33					

the stabilizing effects of the magnetic field are less influential in the development of KHI, and a larger solid angle is thus unstable to the growth of the KHI.

A cluster of KHI events occur at high southern magnetic latitudes ( $\text{GSM-Z} < -4.5R_E$ ), showing the KHI is not limited to lower latitudes. This is a new finding, as previous missions, such as THEMIS, remained at lower magnetic latitudes. Only three prior studies, two using Cluster data [Hwang *et al.*, 2012; Ma *et al.*, 2016], and one using MMS data [Nykyri *et al.*, 2021; Michael *et al.*, 2021] (marked with asterisk in Table 2), have been conducted on the KHI at high latitudes near the dawn and dusk flanks of the high-altitude cusps.

Figure 5 depicts the GR (top), UGR (middle), and USA (bottom), of 44 of the 45 events as a function of SW density (far left), temperature (center left), flow speed (center), Alfvén Mach number (center right), and IMF magnitude (far right) taken from OMNI data. OMNI data was not available for one event. The color bar indicates the event number, so each event is shown with the same color in all plots for direct comparison.

SW density ranges from 2.6 to 17.0 /cc. Observed events are well distributed over the density range, and no relationship is apparent between density and GR or USA. Temperatures generally range from 0.7 to 31.4 eV, with one outlier event occurring with a SW temperature of 61.0 eV. Most events are observed for SW temperatures less than 20 eV, but no trend in GR, UGR, or USA is apparent.

There is an apparent selection window in the solar wind flow speed, with all events occurring when solar wind flow is between 295 and 610 km/s. This fits with expectations that low velocity shears between the sheath and magnetosphere are not unstable to the KHI, and compressibility effects for very large shears stabilize the KHI [Miura and Pritchett, 1982]. Within this selection window there is no correlation between SW flow speed and GR, UGR, or USA. Alfvén Mach numbers also show no clear relationship to GR, UGR, or USA. Events are observed for Alfvén Mach numbers between 3.8 and 26.3, though most events occur when the Mach Number is below 20.

IMF magnitude for all but one event is greater than 1.5 nT and less than 11.2 nT. The outlier event occurred for an average IMF magnitude of 20.8 nT [Eriksson *et al.*, 2016]. Events are otherwise evenly distributed throughout the range of IMF magnitudes with no apparent relationship to GR, UGR or USA.

468 We also compare the solar wind conditions for which KHI is observed to the solar  
 469 wind conditions throughout the entire 4.5 year interval from September 2015 to March  
 470 2020 in Figure 6. MMS observes KHI for the full range of solar wind conditions. Den-  
 471 sity, temperature, flow speed, and Alfvén Mach number values during KH intervals oc-  
 472 cur with similar frequency as in the full time range with only slight deviations. The most  
 473 pronounced difference is in SW flow speed. KHI intervals overrepresent high SW speeds,  
 474 particularly between 350 and 450 km/s. This is unsurprising, as KH develop preferen-  
 475 tially for high ( $> 400$  km/s) SW speeds and compressibility at very high speeds ( $> 600$   
 476 km/s) can have a stabilizing effect. Given the distribution of SW speeds during the 4.5  
 477 year interval, the apparent selection window in SW speed is probably not significant, as  
 478 the solar wind speed is not often below 300 km/s or above 600 km/s.

483 As can be seen in Figure 7, IMF magnitude during KH intervals is nearly identi-  
 484 cal to the observations in the complete time range, with a small decrease around the most  
 485 common strength and an increase at very large IMF (this is due to the outlier event oc-  
 486 ccurring for  $\text{IMF} \approx 20$  [Eriksson *et al.*, 2016]). The planar IMF components show no sig-  
 487 nificant or conclusive variation from the full time range to the KHI intervals. For the  $B_Z$   
 488 component of the IMF, KHI intervals tend to occur more for NIMF than southward IMF  
 489 (SIMF). This is likely due to subsolar reconnection during SIMF, which creates a more  
 490 diffuse boundary layer which is less prone to the development of the KHI.

494 The SW conditions and IMF orientations help explain the observation of more KHI  
 495 on the dusk side of the magnetopause than on the dawn side. Henry *et al.* [2017] found  
 496 dusk flank formation to be more common both for high SW speeds ( $> 400$  km/s) and  
 497 NIMF orientations. 25 of the 45 events occur when SW speed was high, and 29 of the  
 498 45 events had IMF orientations with positive  $B_Z$  components.

#### 499 **4 Comparison with Simulations**

500 To verify our method of isolating regions on either side of the boundary is robust,  
 501 it was applied to parameters generated by two dimensional MHD simulations of the KHI.  
 502 A simulation case for a KHI developing under NIMF conditions was tested using initial  
 503 conditions comparable to those of the event on 08 September 2015. A second simulation  
 504 case used initial conditions similar to those of the 18 October 2015 event for the KHI  
 505 developing on the dusk flank under Parker Spiral IMF (PSIMF) orientation.

506 The simulations, after *Ma et al.* [2019], solve the full set of resistive Hall-MHD equa-  
 507 tions using a leapfrog scheme [*Potter*, 1973; *Birn*, 1980; *Otto*, 1990]. We normalize all  
 508 physical quantities to their typical scale, for example, the length  $L$  is normalized to  $L_0$ ,  
 509 the half width of the initial sheared flow; number density to  $n_0$ , the magnetic field to  $B_0$ ,  
 510 velocity to the Alfvén velocity,  $v_A = B/\sqrt{\mu_0\rho_0}$ ; and the time to the Alfvén transit time  
 511  $T_A = L_0/v_A$ . Exact values of the normalizations for both simulation cases are listed  
 512 in the Supplement.

513 A cut is taken through the simulation box at every time step. Data from these cuts  
 514 are separated into distinct regions using the method described in Section 2.4, then used  
 515 to calculate GR and USA. The GR as a function of time is shown in blue in panel (a)  
 516 of Figures 8 and 9 for the NIMF and PSIMF cases respectively. The GR of the obser-  
 517 vation case on which the simulations are based is also shown in black, and the simula-  
 518 tion GR, as determined by the slope of the linear portion a plot of  $\ln(v_\perp)$  as a function  
 519 of time, is shown in green. Examples of the density at various time steps show the de-  
 520 velopment of the KHI (panels b-f). The cuts used for calculations are shown in red in  
 521 the same panels.

533 As can be seen in Figures 8 and 9, the KHI growth rate increased from its initial  
 534 value until the cut through the simulation captured vortex roll-over. After roll-over is  
 535 observed, growth rate decreases sharply then increases towards its initial level as the in-  
 536 stability dissipates. All of this is consistent with expectations: the free energy available  
 537 to drive the KHI peaks before the vortex forms. The KHI then dissipates the energy.

538 In the NIMF case, GR calculated using Equation 2 are significantly greater than  
 539 the simulation GR. This is to be expected as Equation 2 assumes an infinitely thin bound-  
 540 ary layer and incompressible plasma; the simulation GR is free from these assumptions.  
 541 In contrast, the simulation GR is larger, though very near, than the GR determined us-  
 542 ing Equation 2 for the PSIMF case. This may be due to other assumptions made in the  
 543 simulation (e.g. pressure is not constant, beta is smaller than observed).

544 Within the first few time steps, the simulation matches well with the observed GR  
 545 for the NIMF case. The GR of the event the NIMF simulation is based on is 81.63 km/s.  
 546 The initial GR for the simulation is 82.74 km/s, and remains within 5 km/s of the ob-  
 547 served GR for more than 80 time steps. That is, the first 20% of the simulation is in rough  
 548 agreement with the observation.

549 The PSIMF simulation shows equally good, if not better, agreement with the ob-  
 550 served event on which it is based. The observed event has a GR of 52.41 km/s, and the  
 551 initial GR value for the simulation is 52.44 km/s. The GR of the simulation remains within  
 552 5 km/s of the observation’s GR for more than 230 time steps, or nearly 60% of the sim-  
 553 ulation.

554 We note the growth rate is dependent upon the geometry of the cut. The method  
 555 of separating the two regions works best when the spacecraft spends a significant por-  
 556 tion of the event duration on both sides of the boundary. Therefore, events in which MMS  
 557 only skims the KHI or spends significantly more time in one region than the other may  
 558 actually grow faster than our calculations would indicate. The dependence of GR on cut  
 559 geometry are discussed in more detail in the Supplementary Information.

## 560 **5 Conclusions and Discussion**

561 The main conclusions may be summarized as follows:

- 562 • MMS observed 45 clear KHI events from September 2015 to March 2020.

563 From September 2015 to March 2020 MMS observed more than 100 unique mixed  
 564 regions which initially resembled the KHI. Further analysis of total pressure and boundary-  
 565 normal rotated magnetic field showed 45 of these events likely to be the KHI. These 45  
 566 events, summarized in Table 1, occur under a variety of prevailing SW conditions and  
 567 IMF orientations.

568 The 45 events presented here form the beginnings of a database for statistical stud-  
 569 ies of the KHI and its associated secondary processes. Burst mode data is available for  
 570 portions of all the identified events. This is useful and necessary for future studies of sec-  
 571 ondary processes approaching the electron scale. The methods used here may also be  
 572 applied to the MMS data from April 2020 to present to further extend the database of  
 573 events for analysis.

- 574 • An automated method uses  $nv_{tail}/T$  and specific entropy to identify the magne-  
 575 tosheath and magnetospheric regions, respectively, within a KH wave event. This  
 576 method consistently isolates the pure regions, and excludes mixed plasma, both  
 577 for real satellite and simulated data.

578 The identified magnetosheath and magnetospheric regions of each KHI event match  
 579 well with the omni-directional ion energy spectrogram and density and temperature time  
 580 series. Mean values of density, temperature, velocity, and magnetic field in the identi-  
 581 fied regions are consistent with expectations. Plots of the GSM- $X$  velocity and density  
 582 show mixed regions are successfully avoided. See the Supplementary Information for more  
 583 details on the development of the presented method and rejected alternatives.

584 In simulations the density within the identified regions throughout the simulation  
 585 is within 0.15/cc of the initial value for the NIMF case and 0.25/cc of the initial value  
 586 for the PSIMF case. Thus our method of isolating the pure magnetosheath and mag-  
 587 netosphere is reliable and robust even for late stage KHI with roll-over and mixing.

588 When comparing the results of the simulation and the observation, we see good agree-  
 589 ment for the growth rate for the NIMF and PSIMF case. GR from the NIMF simula-  
 590 tion was within 5 km/s agreement with the observational case for  $\approx 20\%$  of the simu-  
 591 lation, and the PS simulation was in agreement for nearly 60% of the simulation.

- 592 • Plasma parameters from the automatically isolated regions were used to calculate  
 593 KHI GR, UGR, and USA for the 45 KHI events in our database.

594 GR, UGR normalized to the local fast mode speed, and USA for the 45 KHI events  
 595 in our database are reported in Table 2.

596 Growth rates range from a minimum of 3.93 to 103.16 km/s. When normalized to  
 597 the fast mode speed, the unitless growth rate ranges from 0.005 to 0.325 in the extremes,  
 598 with most events in the 0.01 to 0.20 range. That is, most of the observed KHI grow at  
 599 a speed that is between 1% and 20% of the local fast mode speed.

600 Two of the events have unstable solid angles less than 1% of the total  $4\pi$  solid an-  
 601 gle. Unstable solid angles are between 1% and 10% for 23 events, and between 10% and  
 602 25% for 17 events. Three events have unstable solid angles greater than 25% of the to-  
 603 tal  $4\pi$  solid angle. Larger solid angles are more common further down tail where the ve-  
 604 locity shear from the magnetosheath to the magnetosphere is greater and thus the sta-  
 605 bilizing effects of the magnetic field are less influential.

606 We note a few of the observed events occur in apparently stable regions with very  
 607 low growth rates (e.g: the high-latitude case on 25 Feb 2016 [*Nykyri et al., 2021; Michael*

608 *et al.*, 2021]; this does not preclude the observed events from being the KHI. Convective  
 609 instabilities, like the KHI, dissipate energy stored in unstable regions and systems. As  
 610 excess energy is dissipated, the region becomes more stable, thus maximum instability  
 611 and growth rates occur just prior to the formation of the instability. Because it is dif-  
 612 ficult to identify the KHI in observational data until is relatively well developed and has  
 613 dissipated some of the excess free energy, observations will only be made after growth  
 614 rates have decreased from their maxima. We believe those events occurring in apparently  
 615 more stable regions may be later in development than faster growing KHI in less stable  
 616 areas.

617 We also note the path MMS takes through the KHI event can have a significant  
 618 effect on the growth rate determination. Encounters which merely skim the KH vortex  
 619 rather than passing directly through it may actually grow faster than our calculations  
 620 would indicate.

- 621 • The KHI is observed when SW flow speeds are between 295 and 610 km/s. Within  
 622 this flow speed selection window, KHI GR, UGR, and USA are independent of pre-  
 623 vailing SW conditions.

624 Values of the GR, UGR, and USA for each event are listed in Table 2. As can be  
 625 seen in Figure 5, GR, UGR, and USA appear to be independent of SW conditions, with  
 626 the exception of SW flow speed. All of the observed events occurred when the SW speed  
 627 was between 295 and 610 km/s. At flow speeds much below 295 km/s the velocity shear  
 628 is too low to satisfy the KHI onset conditions (Equation 1). At SW speeds above 610  
 629 km/s the compressibility of the plasma will usually stabilize the KHI [*Miura and Pritch-*  
 630 *ett*, 1982]. Within this selection window between 295 and 610 km/s however, flow speed  
 631 is not correlated with GR, UGR, or USA. However, as can be seen in Figure 6, this se-  
 632 lection window may reflect the distribution of SW speed throughout the entire 4.5 year  
 633 time range considered in this study.

634 The database of MMS KHI observations presented here will be used in future stud-  
 635 ies of secondary processes associated with the KHI. The availability of burst mode data  
 636 for all 45 events allows studies of secondary KHI processes to be extended to smaller spa-  
 637 tial and temporal scales. The trends we have observed in the location and SW and IMF

638 conditions may also be used to simplify the search for and identification of future KHI  
 639 events.

## 640 **Acknowledgments**

641 Funding for this work was provided by the National Science Foundation under grant num-  
 642 ber 1707521 and by NASA under grants numbers NNZ17AI50G and NNX16AF89G. Thanks  
 643 are owed to the entire MMS team, and especially to the FGM and FPI instrument groups.  
 644 MMS data was retrieved from the MMS Science Data Center at [lasp.Colorado.edu/mms/sdc/public](http://lasp.Colorado.edu/mms/sdc/public).  
 645 OMNI solar wind data is available from NASA Goddard Space Flight Center’s Space Physics  
 646 Data Facility at [omniweb.gsfc.nasa.gov](http://omniweb.gsfc.nasa.gov).

## 647 **References**

- 648 Adamson, E., K. Nykyri, and A. Otto (2016), The Kelvin-Helmholtz instability un-  
 649 der Parker-spiral interplanetary magnetic field conditions at the magnetospheric  
 650 flanks, *Advances in Space Research*, *58*.
- 651 Axford, W., and C. Hines (1961), A unifying theory of high-Latitude phenomena  
 652 and geomagnetic storms, *Canadian Journal of Physics*, *39*, 1433–1464.
- 653 Birn, J. (1980), Computer studies of the dynamic evolution of the geomagnetic tail,  
 654 *Journal of Geophysical Research*, *85*, 1214–1222.
- 655 Burch, J. L., and T. D. Phan (2016), Magnetic reconnection and the dayside mag-  
 656 netopause: advances with MMS, *Geophysical Research Letters*, *43*, 8327–8338,  
 657 doi:10.1002/2016GL069787.
- 658 Burch, J. L., T. E. Moore, R. B. Torbert, and B. L. Giles (2016), Magnetospheric  
 659 Multiscale overview and science objectives, *Space Science Reviews*, *199*, 5–21,  
 660 doi:10.1007/s11214-015-0164-9.
- 661 Burkholder, B. L., K. Nykyri, X. Ma, R. Rice, S. A. Fuselier, K. J. Trattner, K. R.  
 662 Pritchard, J. L. Burch, and S. M. Petrinec (2020), Magnetospheric multiscale ob-  
 663 servation of an electron diffusion region at high latitudes, *Geophysical Research*  
 664 *Letters*, *47*(15), doi:10.1029/2020GL087268.
- 665 Chandrasekhar, S. (1961), *Hydrodynamic and Hydromagnetic Stability*, Oxford Uni-  
 666 versity Press.
- 667 Chaston, C. C., M. Wilber, M. Fujimoto, M. L. Goldstein, M. Acuna, H. Réme,  
 668 and A. Fazakerley (2007), Mode conversion of anomalous transport in Kelvin-

- 669 Helmholtz vortices and kinetic Alfvén waves at Earth’s magnetopause, *Physical*  
 670 *Review Letters*, *99*.
- 671 Dimmock, A. P., and K. Nykyri (2013), The statistical mapping of magnetosheath  
 672 plasma properties based on THEMIS measurements in the magnetosheath in-  
 673 terplanetary medium reference frame, *Journal of Geophysical Research*, *118*,  
 674 4963–4876.
- 675 Dimmock, A. P., K. Nykyri, H. Karimabadi, A. Osmane, and T. I. Pulkkinen  
 676 (2015), A statistical study into the spatial distribution and dawn-dusk asym-  
 677 metry of dayside magnetosheath ion temperatures as a function of upstream  
 678 solar wind conditions, *Journal of Geophysical Research*, *120*, 2767–2782, doi:  
 679 10.1002/2014JA020734.
- 680 Eriksson, S., B. Lavraud, F. D. Wilder, J. E. Stawarz, B. L. Giles, J. L. Burch,  
 681 W. Baumjohann, R. E. Ergun, P.-A. Lindqvist, W. Magnes, C. J. Pollock, C. R.  
 682 Russel, Y. Saito, R. J. Strangeway, R. B. Torbert, D. J. Gershmann, Y. V.  
 683 Khotyaintsev, J. C. Dorelli, S. J. Schwartz, L. Avanov, E. Grimes, Y. Vernisses,  
 684 A. P. Sturmer, T. D. Phan, G. T. Marklund, T. E. Moore, W. R. Paterson, and  
 685 K. A. Goodrich (2016), Magnetospheric multiscale observations of magnetic recon-  
 686 nection associated with Kelvin-Helmholtz waves, *Geophysical Research Letters*, *43*,  
 687 5606–5615, doi:10.1002/2016GL068783.
- 688 Fairfield, D. H., A. Otto, T. Mukai, S. Kokubun, R. P. Lepping, J. T. Steinberg,  
 689 A. J. Lazaurs, and T. Yamamoto (2000), Geotail observations of the Kelvin-  
 690 Helmholtz instability at the equatorial magnetotail boundary for parallel north-  
 691 ward fields, *Journal of Geophysical Research*, *105*.
- 692 Foullon, C., C. J. Farrugia, A. N. Fazakerley, C. J. Owen, F. T. Gratton, and R. B.  
 693 Torbert (2008), Evolution of Kelvin-Helmholtz activity on the dusk flank magne-  
 694 topause, *Journal of Geophysical Research*, *113*, doi:10.1029/2008JA013175.
- 695 Gosling, J. T., M. F. Thomsen, S. J. Bame, and C. T. Russell (1986), Accelerated  
 696 plasma flows at the near-tail magnetopause, *Journal of Geophysical Research:*  
 697 *Space Physics*, *91*, doi:10.1029/JA091iA03p03029.
- 698 Hasegawa, H., M. Fujimoto, K. Maezawa, Y. Saito, and T. Mukai (2003), Geotail  
 699 observation of the dayside outer boundary region: Interplanetary magnetic field  
 700 control and dawn-dusk asymmetry, *Journal of Geophysical Research*, *108*, doi:  
 701 10.1029/2002JA009667.

- 702 Hasegawa, H., M. Fujimoto, T.-D. Phan, H. Réme, A. Balogh, M. W. Dunlop,  
 703 C. Hashimoto, and R. TanDokoro (2004), Transport of solar wind into Earth's  
 704 magnetosphere through rolled-up Kelvin-Helmholtz vortices, *Nature*, *430*, 755–758.
- 705 Hasegawa, H., M. Fujimoto, K. Takagi, Y. Saito, T. Mukai, and H. Réme (2006),  
 706 Single-spacecraft detection of rolled-up Kelvin-Helmholtz vortices at the flank  
 707 magnetopause, *Journal of Geophysical Research*, *111*, doi:10.1029/2006JA011728.
- 708 Hasegawa, H., A. Retinò, A. Vaivads, Y. Khotyaintsev, M. Andre, T. K. M. Naka-  
 709 mura, L.-L. Teh, B. U. O. Sonnerup, S. J. Schwartz, Y. Seki, M. Fujimoto,  
 710 Y. Saito, H. Reme, and P. Canu (2009), Kelvin-Helmholtz waves at the Earth's  
 711 magnetopause: multiscale development and associated reconnection, *Geophysical*  
 712 *Research Letters*, *114*, doi:10.1029/2009JA014042.
- 713 Henry, Z. W., K. Nykyri, T. W. Moore, A. P. Dimmock, and X. Ma (2017), On the  
 714 dawn-dusk asymmetry of the Kelvin-Helmholtz instability between 2007 and 2013,  
 715 *Journal of Geophysical Research*, *122*, 11,888–11,900, doi:10.1002/2017JA024548.
- 716 Hwang, K.-J., M. L. Goldstein, M. M. Kuznetsova, Y. Wang, A. F. Viñas, and  
 717 D. G. Sibeck (2012), The first in situ observation of kelvin-helmholtz waves at  
 718 high-latitude magnetopause during strongly dawnward interplanetary magnetic  
 719 field conditions, *Journal of Geophysical Research: Space Physics*, *117*(A8), doi:  
 720 10.1029/2011JA017256.
- 721 Johnson, J. R., C. Z. Cheng, and P. Song (2001), Signatures of mode conversion and  
 722 kinetic Alfvén waves at the magnetopause, *Geophysical Research Letters*, *28*.
- 723 Kavosi, S., and J. Reader (2015), Ubiquity of Kelvin-Helmholtz waves at the Earth's  
 724 magnetopause, *Nature Communications*.
- 725 King, J. H., and N. E. Papitashvili (2005), Solar wind spatial scales in and com-  
 726 parisons of hourly wind and ACE plasma and magnetic field data, *Journal of*  
 727 *Geophysical Research*, *110*, doi:10.1029/2004JA010649.
- 728 Li, W., M. Andre, Y. V. Khotyaintsev, A. Vaivads, D. B. Graham, S. Toledo-  
 729 Redondo, C. Norgren, P. Henri, C. Wang, B. B. Tang, B. Lavraud, Y. Vernisse,  
 730 D. L. Turner, J. Burch, R. Torbet, W. Magnes, C. T. Russell, J. B. Blake,  
 731 B. Mauk, B. Giles, C. Pollock, J. Fennell, A. Jaynes, L. A. Avanov, J. C. Dorellie,  
 732 D. J. Gershman, W. R. Paterson, Y. Saito, and R. J. Strangeway (2016), Kinetic  
 733 evidence of magnetic reconnection due to Kelvin-Helmholtz waves, *Geophysical*  
 734 *Research Letters*, *43*, 5635–5643, doi:10.1002/2016GL069192.

- 735 Lin, D., C. Wang, W. Li, B. Tang, X. Guo, and Z. Peng (2014), Properties of  
 736 Kelvin-Helmholtz waves at the magnetopause under northward interplanetary  
 737 magnetic field: statistical study, *Journal of Geophysical Research: Space Physics*,  
 738 *119*, 7485–7494, doi:10.1002/2014JA020379.
- 739 Ma, X., A. Otto, and P. Delamere (2014a), Interaction of magnetic reconnection  
 740 and Kelvin-Helmholtz modes for large magnetic shear: 1. Kelvin-Helmholtz  
 741 trigger, *Journal of Geophysical Research: Space Physics*, *119*, 781–797, doi:  
 742 10.1002/2013JA019224.
- 743 Ma, X., A. Otto, and P. Delamere (2014b), Interaction of magnetic reconnection and  
 744 Kelvin-Helmholtz modes for large magnetic shear: 2. reconnection trigger, *Journal*  
 745 *of Geophysical Research: Space Physics*, *119*, 808–820, doi:10.1002/2013JA019225.
- 746 Ma, X., A. Otto, P. A. Delamere, and H. Zhang (2016), Interaction between recon-  
 747 nection and Kelvin-Helmholtz at the high-latitude magnetopause, *Advances in*  
 748 *Space Research*, *58*(2), 231–239.
- 749 Ma, X., P. Delamere, A. Otto, and B. Burkholder (2017), Plasma transport driven  
 750 by the three-dimensional Kelvin-Helmholtz instability, *Journal of Geophysical*  
 751 *Research: Space Physics*, *122*, 10,382–10,395, doi:10.1002/2017JA024394.
- 752 Ma, X., P. Delamere, K. Nykyri, B. Burkholder, D. Neupane, and R. Rice (2019),  
 753 Comparison between fluid simulation with test particles and hybrid simulation for  
 754 the Kelvin-Helmholtz instability, *Journal of Geophysical Research: Space Physics*,  
 755 *124*, 6654–6668, doi:10.1029/2019JA026890.
- 756 Merkin, V. G., J. G. Lyon, and S. G. Claudepierre (2013), Kelvin-Helmholtz in-  
 757 stability of the magnetospheric boundary in a three-dimensional global MHD  
 758 simulation during northward IMF conditions, *Journal of Geophysical Research:*  
 759 *Space Physics*, *118*, 5478–5496, doi:10.1002/jgra.50520.
- 760 Michael, A. T., K. A. Sorathia, V. G. Merkin, K. Nykyri, B. L. Burkholder, X. Ma,  
 761 A. Y. Ukhorskiy, and J. Garretson (2021), Modeling Kelvin-Helmholtz Instabil-  
 762 ity at the High-Latitude Boundary Layer in a Global Magnetosphere Simulation,  
 763 *Geophysical Research Letters*, *48*(19), doi:10.1029/2021GL094002.
- 764 Miura, A. (1984), Anomalous transport by magnetohydrodynamic Kelvin-Helmholtz  
 765 instabilities in the solar wind-magnetosphere interaction, *Journal of Geophysical*  
 766 *Research*, *89*, 801–818.

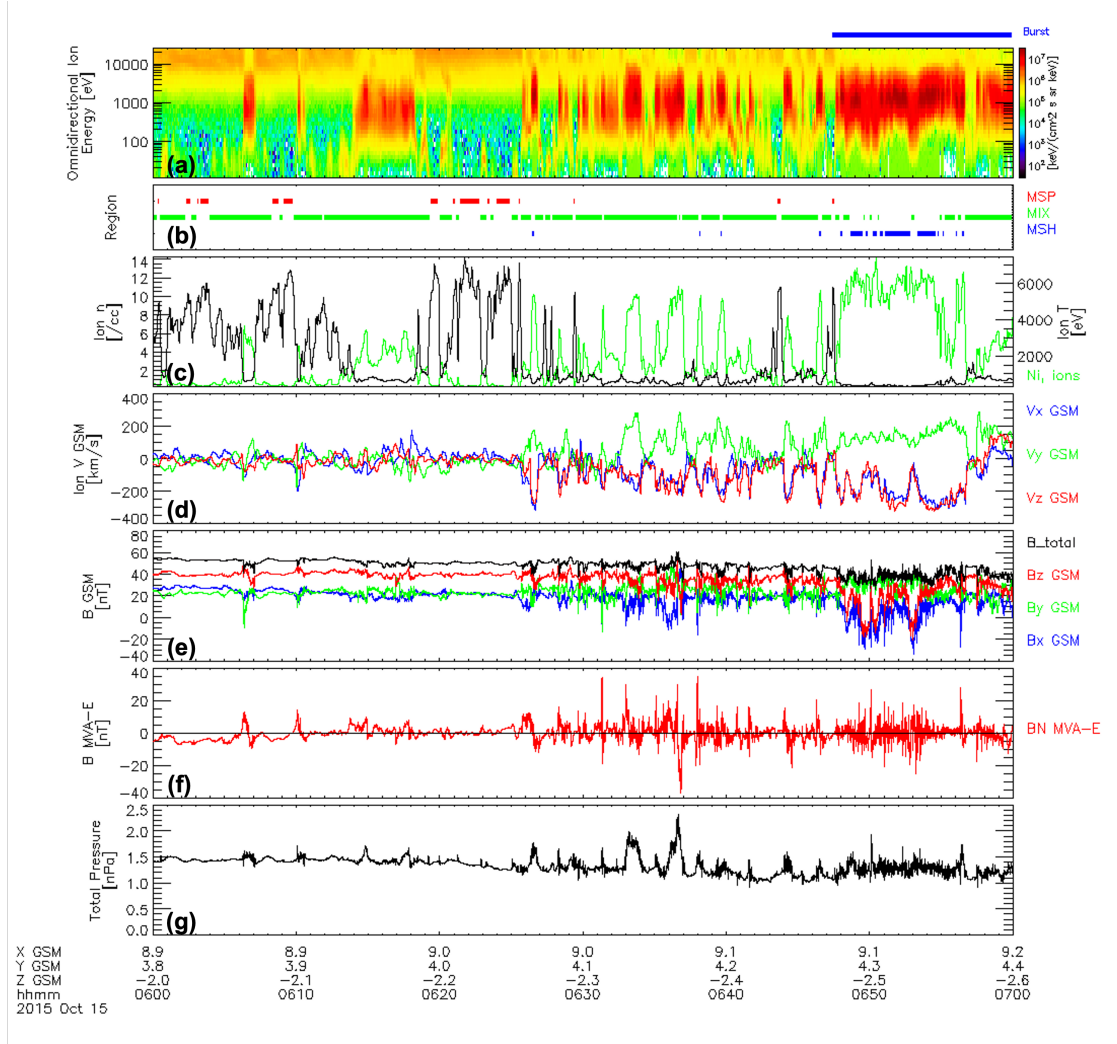
- 767 Miura, A. (1987), Simulation of the Kelvin-Helmholtz instability at the magneto-  
768 spheric boundary, *Journal of Geophysical Research*, *92*, 3195–3206.
- 769 Miura, A., and P. L. Pritchett (1982), Nonlocal stability analysis of the MHD  
770 Kelvin-Helmholtz instability in a compressible plasma, *Journal of Geophysical  
771 Research*, *87*, 7431–7444.
- 772 Moore, T. W., K. Nykyri, and A. P. Dimmock (2016), Cross-scale energy transport  
773 in space plasmas, *Nature Physics*.
- 774 Moore, T. W., K. Nykyri, and A. P. Dimmock (2017), Ion-scale wave properties  
775 and enhanced ion heating across the low-latitude boundary layer during Kelvin-  
776 Helmholtz instability, *Journal of Geophysical Research: Space Physics*, *122*,  
777 11,128–11,153, doi:10.1002/2017JA024591.
- 778 Nykyri, K. (2013), Impact of MHD shock physics on magnetosheath asymmetry and  
779 Kelvin-Helmholtz instability, *Journal of Geophysical Research: Space Physics*, *118*,  
780 5068–5081.
- 781 Nykyri, K., and A. Otto (2001), Plasma transport at the magnetopause boundary  
782 due to reconnection in Kelvin-Helmholtz vortices, *Geophysical Research Letters*,  
783 *28*, 3565–3568.
- 784 Nykyri, K., and A. Otto (2004), Influence of the Hall term on KH instability and  
785 reconnection inside KH vortices, *Annales Geophysicae*, *22*, 935–949.
- 786 Nykyri, K., A. Otto, J. Büchner, B. Nikutowski, W. Baumjohann, L. M. Kistler,  
787 and C. Mouikis (2003), Equator-S observations of boundary signatures: FTE’s  
788 or Kelvin-Helmholtz waves?, in *Earth’s Low-Latitude Boundary Layer, Geophys-  
789 ical Monograph*, vol. 133, edited by P. T. Newell and R. Onsager, pp. 205–210,  
790 American Geophysical Union.
- 791 Nykyri, K., A. Otto, B. Lavraud, C. Mouikis, L. M. Kistler, A. Balogh, and  
792 H. Réme (2006), Cluster observations of reconnection due to the Kelvin-Helmholtz  
793 instability at the dawnside magnetospheric flank, *Annales Geophysicae*, *24*, 2619–  
794 2643.
- 795 Nykyri, K., A. Otto, E. Adamson, and J. Mumme (2011a), Cluster observations of  
796 a cusp diamagnetic cavity: structure, size, and dynamics, *Journal of Geophysical  
797 Research*, *116*, doi:10.1029/2010JA015897.
- 798 Nykyri, K., A. Otto, E. Adamson, and A. Tjulin (2011b), On the origin of fluc-  
799 tuation in the cusp diamagnetic cavity, *Journal of Geophysical Research*, *116*,

- 800 doi:10.1029/2010JA015888.
- 801 Nykyri, K., X. Ma, A. Dimmock, C. Foullon, A. Otto, and A. Osmane (2017), In-  
 802 fluence of velocity fluctuations on the Kelvin-Helmholtz instability and its as-  
 803 sociated mass transport, *Journal of Geophysical Research*, *122*, 9489–9512, doi:  
 804 10.1002/2017JA024374.
- 805 Nykyri, K., X. Ma, B. Burkholder, R. Rice, J. R. Johnson, E.-K. Kim, P. Delamere,  
 806 A. Michael, K. Sorathia, D. Lin, S. Merkin, S. Fuselier, J. Broll, O. Le Contel,  
 807 D. Gershman, I. Cohen, B. Giles, R. J. Strangeway, C. T. Russell, and J. L. Burch  
 808 (2021), MMS observations of the multiscale wave structures and parallel elec-  
 809 tron heating in the vicinity of the southern exterior cusp, *Journal of Geophysical*  
 810 *Research: Space Physics*, *126*(3), doi:10.1029/2019JA027698.
- 811 Otto, A. (1990), 3D resistive MHD computations of magnetospheric physics, *Com-*  
 812 *puter Physics Communications*, *59*, 185–195.
- 813 Otto, A., and D. H. Fairfield (2000), Kelvin-Helmholtz instability at the magnetotail  
 814 boundary: MHD simulation and comparison with Geotail observations, *Journal of*  
 815 *Geophysical Research*, *105*, 21,175–21,190.
- 816 Paschmann, G., B. U. Ö. Sonnerup, I. Papamastorakis, G. Haerendel, S. J. Bame,  
 817 J. R. Asbridge, J. T. Gosling, C. T. Russell, and R. C. Elphric (1979), Plasma  
 818 acceleration at the Earth’s magnetopause: evidence for reconnection, *Nature*, *282*,  
 819 243–246.
- 820 Pollock, C., T. Moore, A. Jacques, J. Burch, U. Gliese, Y. Saito, T. Omoto,  
 821 L. Avanov, A. Barrie, V. Coffey, J. Dorelli, D. Gershman, B. Giles, T. Ros-  
 822 nack, C. Salo, S. Yokota, M. Adrian, C. Aoustin, C. Auletti, S. Aung, V. Bigio,  
 823 N. Cao, M. Chandler, D. Chornay, K. Christian, G. Clark, G. Collinson, T. Cor-  
 824 ris, A. D. L. Santos, R. Devlin, T. Diaz, T. Dickerson, C. Dickson, A. Diekmann,  
 825 F. Diggs, C. Duncan, A. Figueroa-Vinas, C. Firman, M. Freeman, N. Galassi,  
 826 K. Garcia, G. Goodhart, D. Guererro, J. Hageman, J. Hanley, E. Hemminger,  
 827 M. Holland, M. Hutchins, T. James, W. Jones, S. Kreisler, J. Kujawaski, V. Lavu,  
 828 J. Lobell, E. LeCompte, A. Lukemire, E. MacDonald, A. Mariano, T. Mukai,  
 829 K. Narayanan, Q. Nguyen, M. Onizuka, W. Paterson, S. Persyn, B. Piepgrass,  
 830 F. Cheey, A. Rager, T. Raghuram, A. Ramil, L. Reichenthal, H. Rodriguez,  
 831 J. Rouzaud, A. Rucker, Y. Saito, M. Samara, J.-A. Sauvaud, D. Schuster,  
 832 M. Shappirio, K. Shelton, D. Sher, D. Smith, K. Smith, S. Smith, D. Steinfeld,

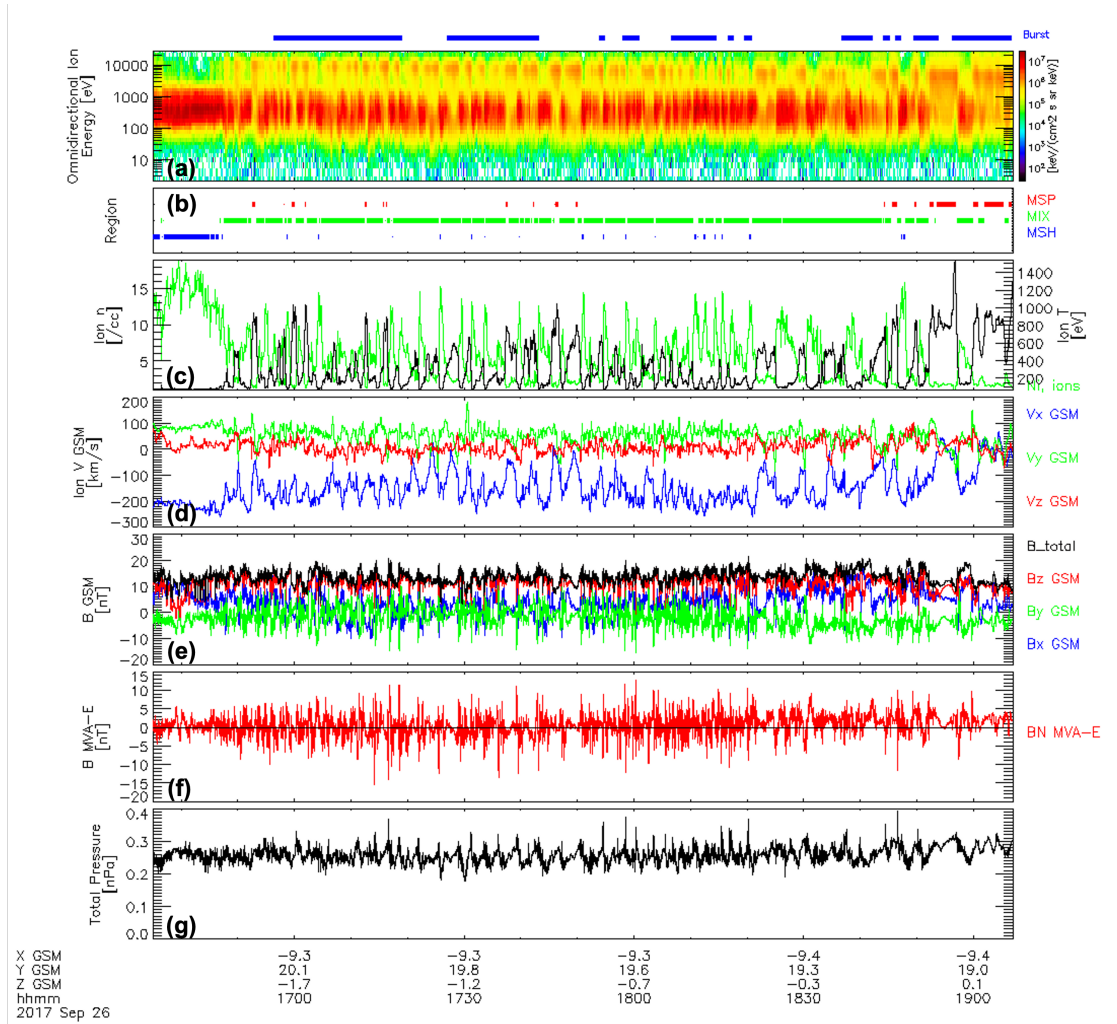
- 833 R. Szymkiewicz, K. Tanimoto, J. Taylor, C. Tucker, K. Tull, A. Uhl, J. Vloet,  
 834 P. Walpole, S. Weidner, D. White, G. Winkert, P.-S. Yeh, and M. Zeuch (2016),  
 835 Fast plasma investigation for Magnetospheric Multiscale, *Space Science Reviews*,  
 836 *199*, 331–406, doi:10.1007/s11214-016-0245-4.
- 837 Potter, D. (1973), *Computational Physics*, John Wiley and Sons.
- 838 Russell, C. T., B. J. Anderson, W. Baumjohann, K. R. Bromund, D. Dearborn,  
 839 D. Fischer, G. Le, H. K. Leinweber, D. Lenema, W. Magnes, J. D. Means, M. B.  
 840 Moldwin, R. Nakamura, D. Pierce, F. Plaschke, K. M. Rowe, J. A. Slavin, R. J.  
 841 Strangeway, R. Torbet, C. Hagen, I. Jernej, A. Valavanoglou, and I. Richter (2016),  
 842 The Magnetospheric Multiscale magnetometers, *Space Science Reviews*, *199*, 189–  
 843 256, doi:10.1007/s11214-014-0057-3.
- 844 Sonnerup, B. U. Ö., and M. Scheible (1998), *Analysis Methods for Multi-Spacecraft*  
 845 *Data*, chap. Minimum and Maximum Variance Analysis, pp. 185–220, Interna-  
 846 tional Space Science Institute.
- 847 Sonnerup, B. U. Ö., G. Paschmann, I. Papamastorakis, N. Sckopke, G. Haerendel,  
 848 S. J. Bame, J. R. Asbridge, J. T. Gosling, and C. T. Russell (1981), Evidence for  
 849 magnetic field reconnection at the Earth’s magnetopause, *Journal of Geophysical*  
 850 *Research: Space Physics*, *86*, doi:10.1029/JA086iA12p10049.
- 851 Sorathia, K. A., V. G. Merkin, A. Y. Ukhorskiy, R. C. Allen, K. Nykyri,  
 852 and S. Wing (2019), Solar wind ion entry into the magnetosphere during  
 853 northward IMF, *Journal of Geophysical Research: Space Physics*, *124*, doi:  
 854 doi.org/10.1029/2019JA026728.
- 855 Stawarz, J. E., S. Eriksson, F. D. Wilder, R. E. Ergun, S. J. Schwartz, A. Pou-  
 856 quet, J. L. Burch, B. L. Giles, Y. Khotyaintsev, O. L. Contel, P.-A. Lindqvist,  
 857 W. Magnes, C. J. Pollock, C. T. Russell, R. J. Strangeway, R. B. Torbert, L. A.  
 858 Avanov, J. C. Dorelli, J. P. Eastwood, D. J. Gershman, K. A. Goodrich, D. M.  
 859 Malaspina, G. T. Marklund, L. Mirioni, and A. P. Sturmer (2016), Observations  
 860 of turbulence in a Kelvin-Helmholtz event on 8 September 2015 by the Magneto-  
 861 spheric Multiscale mission, *Journal of Geophysical Research*, *121*, 11,021–11,034,  
 862 doi:10.1002/10JA023458.
- 863 Taylor, M. G. G. T., B. Lavraud, C. P. Escoubet, S. E. Milan, K. Nykyri, M. W.  
 864 Dunlop, J. A. Davies, R. H. W. Friedel, H. Frey, Y. V. Bogdanova, A. Asnes,  
 865 H. Laasko, P. Trvincek, A. Masson, H. Opgenoorth, C. Vallat, A. N. Fazaker-

- 866 ley, A. D. Lahiff, C. J. Owen, F. Pitout, Z. Pu, C. Shen, Q. G. Zong, H. Rme,  
 867 J. Scudder, and T. L. Zhang (2008), The plasma sheet and boundary layers un-  
 868 der northward IMF: a multi-point and multi-instrument perspective, *Advances in*  
 869 *Space Research*, *41*, 1619–1629.
- 870 Taylor, M. G. G. T., H. Hasegawa, B. Lavraud, T. Phan, C. P. Escobet, M. W.  
 871 Dunlop, Y. V. Bogdanova, A. L. Borg, M. Volwerk, J. Berchem, O. D. Constan-  
 872 tinescu, J. P. Eastwood, A. Masson, H. Laakso, J. Soucek, A. N. Fazakerley,  
 873 H. Frey, E. V. Panov, C. Shen, J. K. Shi, D. G. Sibeck, Z. Y. Pu, J. Wang, and  
 874 J. A. Wild (2012), Spatial distribution of rolled up Kelvin-Helmholtz vortices at  
 875 Earth’s dayside and flank magnetopause, *Annales Geophysicae*, *30*, 1025–1035,  
 876 doi:10.5194/angeo-30-1025-2012.
- 877 Torbert, R. B., C. T. Russell, w. Magnes, R. E. Ergun, P.-A. Lindqvist, O. LeCon-  
 878 tel, H. Vaith, J. Macri, S. Myers, D. Rau, J. Needell, B. King, M. Granoff,  
 879 M. Chutter, I. Dors, G. Olsson, Y. V. Khotyaintsev, A. Eriksson, C. A. Klet-  
 880 zing, S. Bounds, B. Anderson, W. Baumjohann, M. Steller, K. Bromund,  
 881 G. Le, R. Nakamura, R. J. Strangeway, H. K. Leinweber, S. Tucker, J. West-  
 882 fell, D. Fisher, F. Plaschke, J. Porter, and K. Lappalainen (2016), The FIELDS  
 883 instrument suite on MMS: scientific objectives, measurements, and data products,  
 884 *Space Science Reviews*, *199*, 105–135, doi:10.1007/s11214=014-0109-8.
- 885 Wilder, F. D., R. E. Ergun, S. J. Schwartz, D. L. Newman, S. Eriksson, J. E.  
 886 Stawarz, M. V. Goldman, K. A. Goodrich, D. J. Gershman, D. M. Malaspina,  
 887 J. C. Holmes, A. P. Sturner, J. L. Burch, R. B. Torbert, P.-A. Lindqvist, G. T.  
 888 Marklund, Y. Khotyaintsev, R. J. Strangeway, C. T. Russel, C. J. Pollock, B. L.  
 889 Giles, J. C. Dorelli, L. A. Avanov, W. R. Patterson, F. Plaschke, and W. Magnes  
 890 (2016), Observations of large-amplitude, parallel, electrostatic waves associated  
 891 with the Kelvin-Helmholtz instability by the Magnetospheric Multiscale mission,  
 892 *Geophysical Research Letters*, *43*, 8859–8866, doi:10.1002/2016GL070404.
- 893 Wing, S., J. R. Johnson, P. T. Newell, and C.-I. Meng (2005), Dawn-dusk asym-  
 894 metries, ion spectra, and sources in the northward interplanetary magnetic field  
 895 plasma sheet, *Journal of Geophysical Research*, *110*, doi:10.1029//2005JA011086.
- 896 Zhao, C., C. T. Russell, R. J. Strangeway, S. M. Petrinec, W. R. Paterson, M. Zhou,  
 897 B. J. Anderson, W. Baumjohann, K. R. Bromund, M. Chutter, D. Fischer,  
 898 G. Le, R. Nakamura, F. Plaschke, J. A. Slavin, R. B. Torbert, and H. Y. Wei

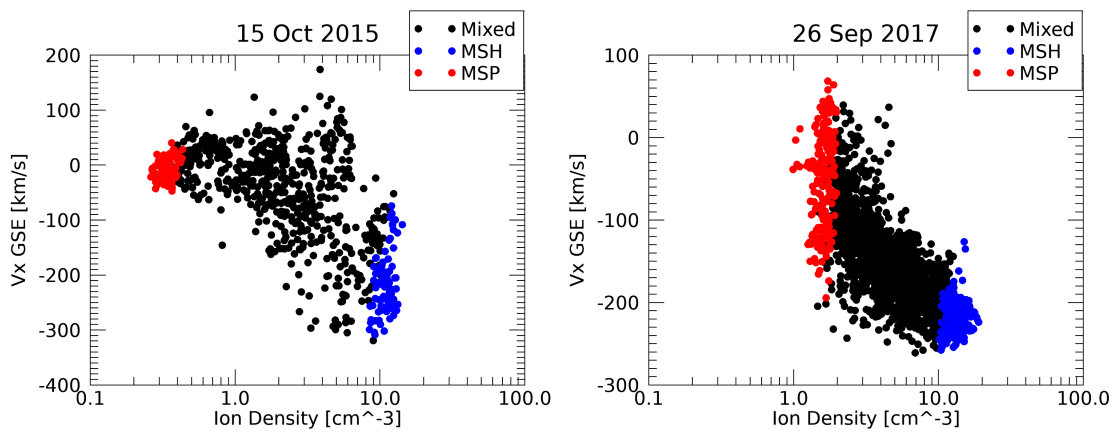
899 (2016), Force balance at the magnetopause determined with MMS: application  
900 to flux transfer events, *Geophysical Research Letters*, *43*, 11,941–11,947, doi:  
901 10.1002/2016GL071568.



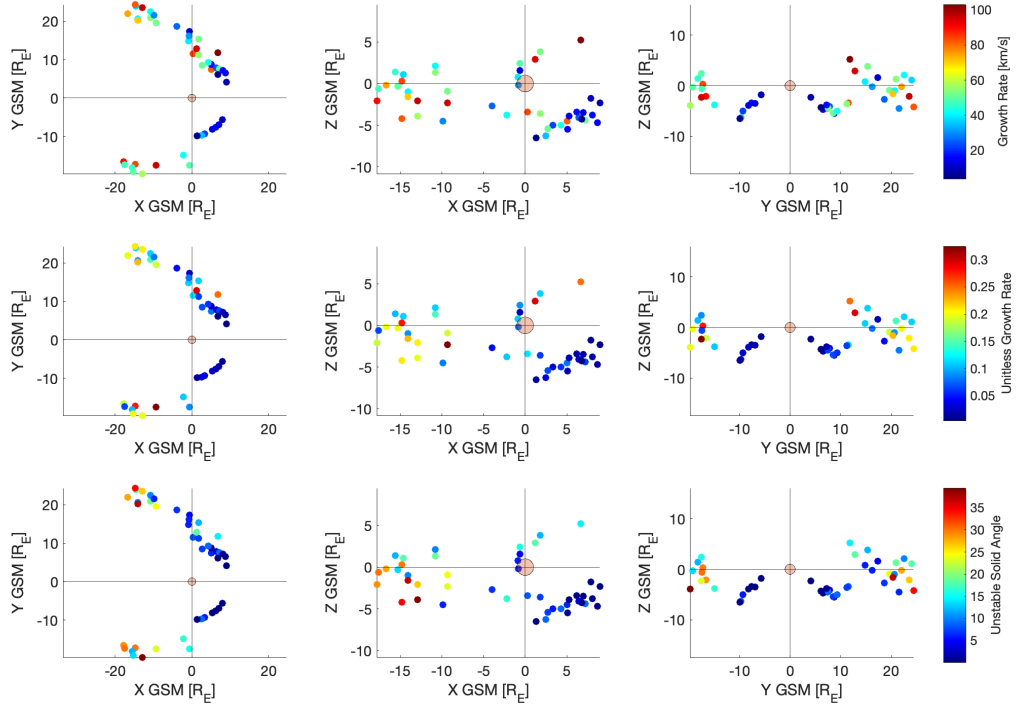
211 **Figure 1.** MMS observations of (a) omnidirectional ion energies; (b) plasma region; (c) ion  
 212 density (green) and temperature (black); (d) ion bulk velocity in GSM coordinates; (e) direct  
 213 current magnetic field in GSM coordinates; (f) the normal component of the magnetic field; and  
 214 (g) total pressure from 06:00 to 07:00 UT on 15 October 2015. Ion data is taken from the Fast  
 215 Plasma Investigation (FPI) and magnetic field data is from the Flux Gate Magnetometer (FGM)  
 216 aboard MMS1. Burst mode data is available for the intervals marked in blue above the panels.



228 **Figure 2.** MMS observations as in Figure 1 from 16:35 to 19:07 UT on 26 September 2017.  
 229 Ion data is taken from the Fast Plasma Investigation (FPI) and magnetic field data is from the  
 230 Flux Gate Magnetometer (FGM) aboard MMS1. Burst mode data is available for the intervals  
 231 marked in blue at top.



324 **Figure 3.** MMS observations of tailward ion velocity as a function of ion density for 06:00-  
 325 07:00 on 15 October 2015 (left) and 16:35-19:07 on 26 September 2017. Blue (red) points were  
 326 identified as magnetosheath (magnetospheric) plasma. Mixed and ambiguous regions are plotted  
 327 in black. For the 2017 example event, ions show clear evidence of roll-over within the KHI vor-  
 328 tex, low density plasma typically associated with the magnetosphere is moving tailward with the  
 329 faster magnetosheath plasma, but this is not seen for the 2015 example event. The overall shape  
 330 of both events however, is consistent with previous studies of the KHI.



426 **Figure 4.** Growth rates (GR, top row), unitless growth rates (UGR, middle row), and  
 427 unstable solid angles (USA, bottom row) plotted with respect to the KHI's location along the  
 428 magnetopause in GSM X-Y plane (left column), X-Z plane (middle column), and Y-Z plane  
 429 (right column).

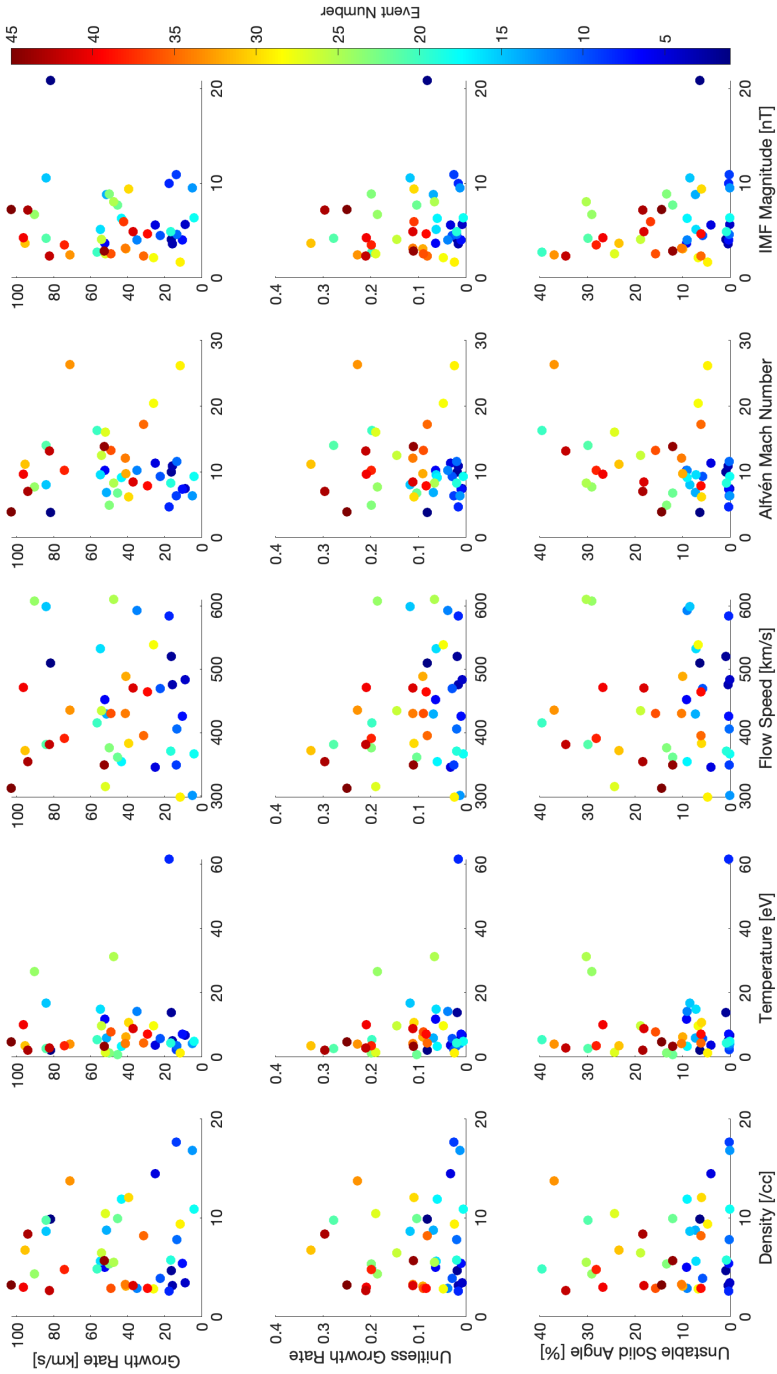
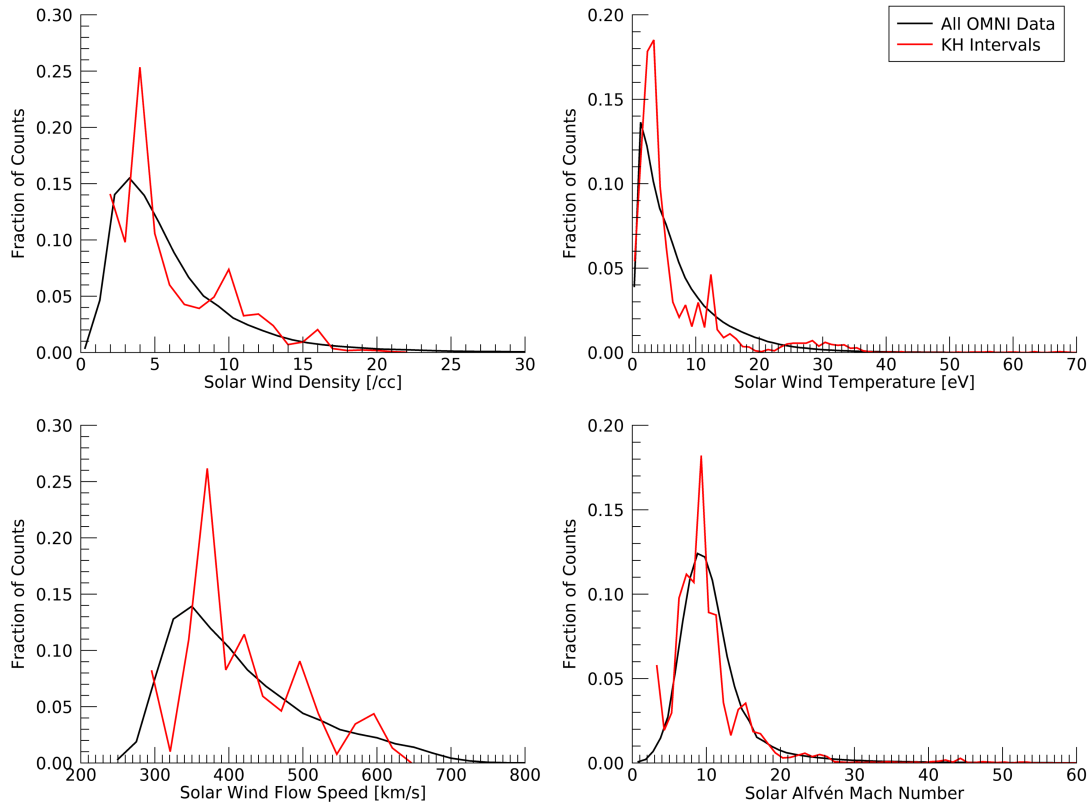
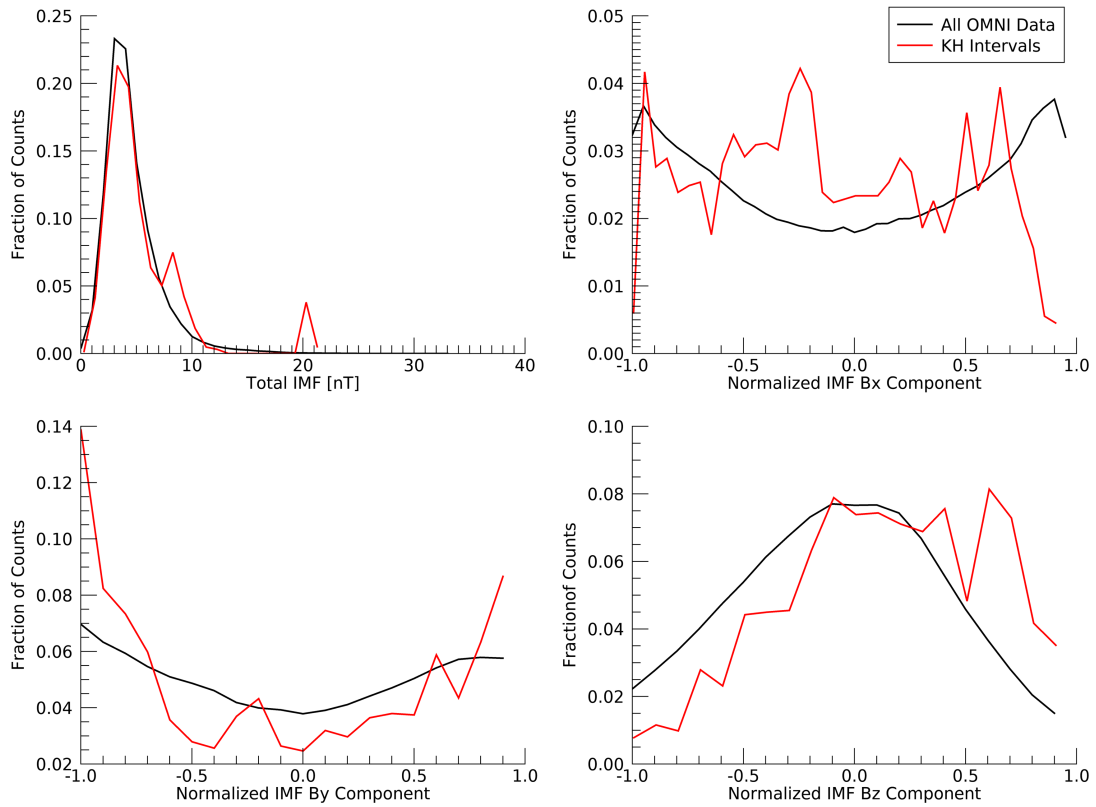


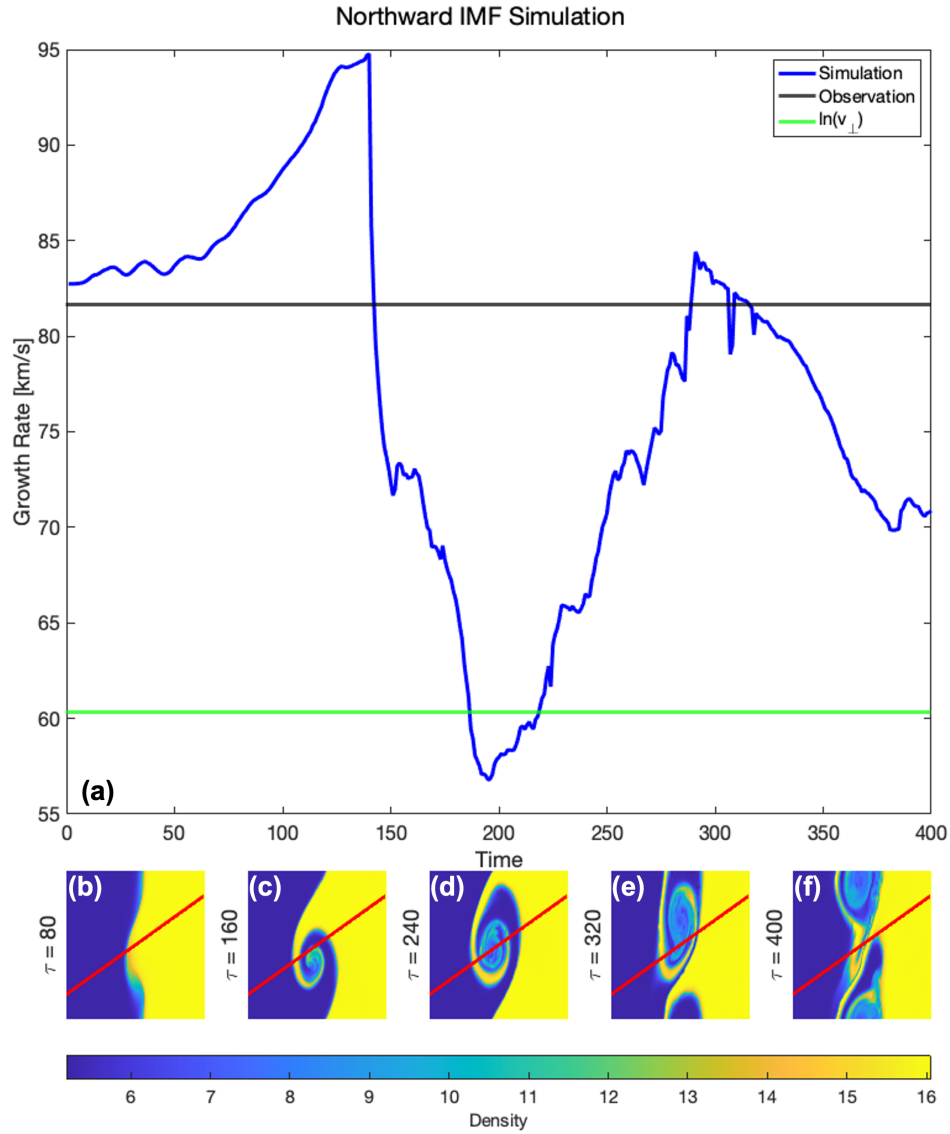
**Figure 5.** KHI growth rates (GR, top), unitless growth rates (UGR, middle), and unstable solid angles (USA, bottom) as a function of SW density (far left), temperature (center left), flow speed (center), Alfvén mach number (center right), and average IMF magnitude (far right). Other than a selection window from 295–610 km/s flow speed, GR, UGR, and USA are independent of solar wind parameters. The color bar indicates each unique event from plot to plot.



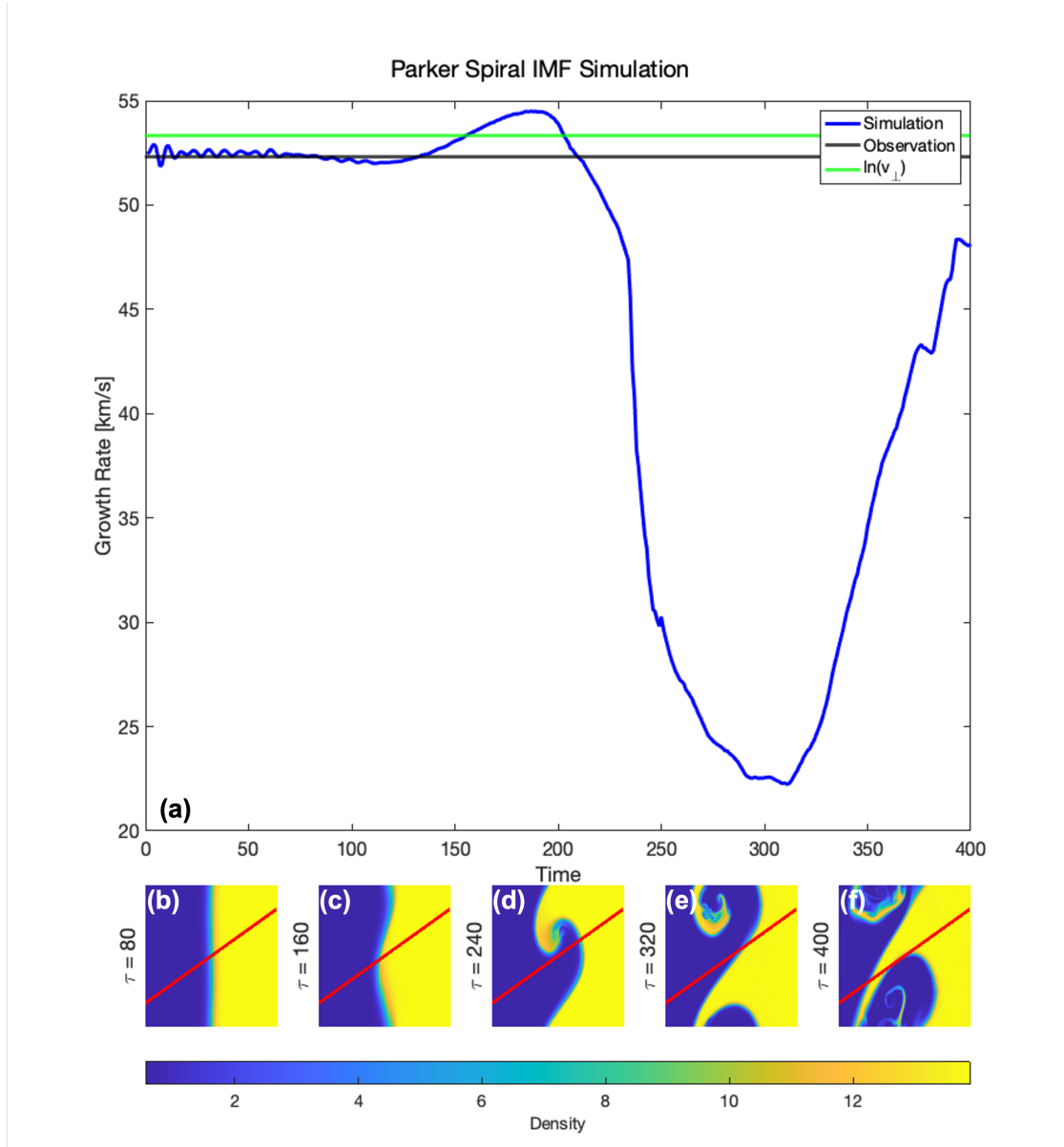
479 **Figure 6.** Normalized histograms of solar wind density (top left), temperature (top right),  
 480 speed (bottom left), and Alfvén Mach number (bottom right) for the complete time range con-  
 481 sidered in this study, 01 September 2015 to 31 March 2020 (black), and for the intervals during  
 482 which MMS observed the KHI (red).



491 **Figure 7.** Normalized histograms of IMF magnitude (top left) and normalized IMF compo-  
 492 nents for the complete time range considered in this study, 01 September 2015 to 31 March 2020  
 493 (black), and for the intervals during which MMS observed the KHI (red).



522 **Figure 8.** Growth rates were calculated and plotted as a function of time (a) using data from  
 523 2D MHD simulations of a dusk flank KHI occurring during Northward IMF. Initial conditions  
 524 of the simulation are based on the event MMS observed on 08 September 2015. Density data  
 525 from several time steps within the simulation (b)-(f) show the development of the KHI. Cuts,  
 526 as indicated by the red line in panels (b)-(f), were taken through the instability at every simu-  
 527 lation time step. The black line (a) indicates the growth rate for the MMS event on which the  
 528 simulation is based. The green line (a) indicates the theoretical growth rate for the simulation as  
 529 determined by the slope of the linear portion of  $\ln(v_{\perp})$  plotted as a function of time.



530 **Figure 9.** The KHI growth rates as in Figure 8 for a 2D MHD simulation of a dusk flank KHI  
 531 occurring during Parker Spiral IMF orientation. Initial conditions of the simulation are based on  
 532 the event MMS observed on 18 October 2015.